Tuning membrane content of sound absorbing cellular foams: Fabrication, experimental evidence and multiscale numerical simulations

van Hai Trinh, Vincent Langlois, Johann Guilleminot, Camille Perrot, Yacine Khidas, Olivier Pitois

Materials and Design 162 (2019) 345–361

Contents lists available at ScienceDirect

Materials and Design

journal homepage: www.elsevier.com/locate/matdes

Tuning membrane content of sound absorbing cellular foams: Fabrication, experimental evidence and multiscale numerical simulations

Van Hai Trinh[a,b], Vincent Langlois[c], Johann Guilleminot[d], Camille Perrot[a,*], Yacine Khidas[e], Olivier Pitois[e]

[a]Université Paris-Est, Laboratoire Modélisation et Simulation Multi Echelle, MSME UMR 8208 CNRS, Marne-La-Vallée 77454, France
[b]Le Quy Don Technical University, Hanoi, Vietnam
[c]Université Paris-Est, Laboratoire Géomatériaux et Environnement (LGE EA 4508), UPEM, Marne-La-Vallée F-77454, France
[d]Department of Civil and Environmental Engineering, Duke University, Durham, NC 27708, USA
[e]Université Paris-Est, Laboratoire Navier, UMR 8205 CNRS, Ecole des Ponts ParisTech, IFSTTAR, 77454 Marne-La-Vallée, France

HIGHLIGHTS

- Monodisperse polymeric foams with tunable membrane content are manufactured.
- Characterizing the proportions and aperture sizes of open windows is required.
- Tuning membranes enables the progressive modification of sound absorbing behavior.
- A microstructural periodic model is able to reproduce membrane-induced effects.
- Tuned membrane content shows interesting specific sound absorbing properties.

GRAPHICAL ABSTRACT

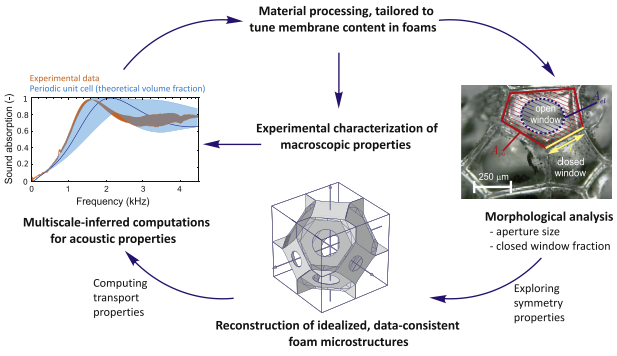

ARTICLE INFO

Article history:
Received 2 August 2018
Received in revised form 8 November 2018
Accepted 8 November 2018
Available online 14 November 2018

Keywords:
Low-density
Porous
Permeability
Foam
Morphology
Fabrication-structure-property

ABSTRACT

This work is focused on tailoring cellular foam membranes for sound absorption. Several foam configurations with a constant porosity and varying membrane content were first fabricated by using milli-fluidic techniques. This approach allows transport and sound absorbing properties to be continuously tuned on purpose, from open-cell to closed-cell foams. The morphology of these foams was then investigated using optical micrography. Microstructural descriptors such as the proportions of closed and open windows and aperture size were specifically analyzed. The associated transport and sound absorbing properties were subsequently characterized using airflow resistivity and three-microphone standing wave tube measurements. The numerical reconstruction of foam samples was next addressed by considering a Periodic Unit Cell (PUC) approach on Kelvin cells. The transport properties of these virtual samples were determined by numerical homogenization, performing sequential evaluations of the parameters that govern visco-thermal losses. To overcome the limitation induced by the size of the numerical model at the pore scale, an averaging procedure was proposed. The results show that the PUC model can be used to accurately predict the transport and sound absorbing behavior of interest. The relevance of the multiscale estimations for acoustic properties is demonstrated over the entire range of membrane content.

* Corresponding author.
E-mail address: camille.perrot@univ-paris-est.fr (C. Perrot).

https://doi.org/10.1016/j.matdes.2018.11.023

1. Introduction

Cellular foams are attractive materials for structural, thermal, acoustical [1,2] and energy absorption [3] applications due to factors such as their low density and high specific surface area properties [4]. Therefore, they have been the focus of much attention during the past three decades [5]. The design of lightweight structures aims, above all, at an optimal compromise between structural properties, transport properties and acoustical performance. Ultimately, the sought-for solution should be compatible with some industrial requirements (large-scale production requirements). The microstructure-informed prediction of some physical properties of interest for a porous medium provides a theoretically sound basis for conducting optimization analyses. It can be approached in various ways, using phenomenological or truly multiscale frameworks on idealized (e.g., periodic) or random foam morphologies. Moreover, crystalline foams, and more particularly those prepared from milli-fluidic techniques, are primary regarded as model systems by physicists, due to their equal-volume pore and well-controlled polymer properties [6]. As such, they may therefore represent a critical step in the understanding of structure-property relations. Here, we report that the acoustical properties of tailored membrane-based cellular foams can be directly determined from numerical homogenization performed on an idealized foam mimicking the microstructure of a real foam.

Even if viscous dissipation is the main loss mechanism, modeling the acoustical properties of a rigid porous medium requires consideration of both visco-inertial and thermal effects [7]. At low frequencies, when the wavelength is much larger than the typical pore size (i.e., scale separation), visco-inertial and thermal effects can be decoupled: the visco-inertial effects are conveniently described by a macroscopically averaged fluid velocity which can be represented at macroscale by a frequency-dependent density [8]; and the thermal effects are described by analogy with a macroscopically averaged fluid temperature represented at macroscale by a frequency-dependent bulk modulus [9]. Then, as long as the scale separation is valid, the dynamic behavior of density and bulk modulus can be approximated by analytic expressions compatible with the low- and high-frequency asymptotic solutions associated with each loss mechanism. Both effects share an intrinsic parameter which is the porosity of the open pore-space, ϕ_{op}. Each mechanism also owns some specific parameters. For visco-inertial effects, three additional parameters have been introduced:

(1) the Darcy static permeability, k_0, related to pore morphology [10] and governing the low frequency behavior of effective density [8];
(2) the tortuosity, α_∞, associated with the high frequency regime for which the flow pattern is identical with that of an ideal fluid, except in the boundary layer (the viscous skin depth becomes much smaller than any characteristic pore size);
(3) the viscous characteristic length, Λ, which is a pore-volume-to-surface ratio of the pore-solid interface in which each area or volume element is weighted according to the local value of the velocity field in the high frequency regime which represents a dynamically connected pore size entering into the analytic properties of the high-frequency limit [8].

Regarding thermal effects, and by analogy with the viscous ones, a further two parameters were added:

(4) the static thermal permeability, k_0', associated with the low frequency regime, which links the pressure time derivative to the macroscopic excess temperature (the excess temperature is equal to the instantaneous temperature minus the equilibrium temperature);
(5) the thermal characteristic length, Λ', which is defined as a generalized hydraulic radius also entering into the analytic properties of the high-frequency limit [11].

At high frequency, the excess temperature is everywhere the same in the pore space because this quantity is related to the adiabatic compression of the air in the material and depends only on the excess pressure that is constant at the pore scale (the excess pressure is equal to the instantaneous pressure minus the equilibrium pressure). In this case, the effective bulk modulus is then equal to the adiabatic bulk modulus and no additional parameter is necessary. All the five previous parameters constituting the input parameters of the Johnson-Champoux-Allard-Lafarge model (JCAL), can be characterized experimentally [12,13]. The relationships between these parameters and the microstructure of porous materials can be inferred in various ways: (A) by considering solutions associated with idealized structures (for example, a network of aligned tubes as in Refs. [7,8,14]), (B) by using semi-empirical relations based on power laws obtained on idealized structures and calibrated on experimental measurements, as done by Gibson et al. [5] for mechanical properties of cellular materials, or by Champoux and Allard for acoustical properties of fibrous materials [15], (C) by the homogenization method [16] performed on numerical periodic structures mimicking the microstructure of a real porous medium. For a porous medium having a complex pore-space, specific tools using mathematical morphology and probability theory were used in order to generate numerical samples that are consistent with observed data from advanced imaging techniques (e.g., micro computed tomography) [17,18]. Finally, as an alternative way to the approach (C) which involves computing only the asymptotic transport parameters, the numerical homogenization method can be used to compute the overall dynamic response functions of the porous medium. The response functions are then related to the visco-thermal effects of interest [18,19].

All of these different approaches have been used to study the acoustical properties of cellular foams. Depending on various factors such as the formulation, processing conditions and post-processing operations [4,20], the microstructures of cellular foams can be characterized by the fraction of closed windows [20,21] or by the degree of opening of membranes [4]. In the case of polyurethane foams, a more complex distribution of membranes is observed which involves both fully closed and partially-open windows [22]. Concerning the acoustical properties, the effect of closed windows was studied by Doutres et al. [20] with a semi-empirical approach (B), and by Park et al. [21] with a numerical homogenization approach (C) performed on a Kelvin cell (tetrakaidecahedron) microstructure. The effect of the window aperture was studied by Hoang et al. [23,24] with the approach (C) performed on a Kelvin structure. By another approach, based on the numerical homogenization of Biot equations, Gao et al. have studied the acoustic properties of foams having both open and closed windows [22]. They have proposed a homogenization model based on a simple mixing law built by parallel association of two types of cells: fully open cells (without any membrane) and partially closed cells. The Biot theory [14] used by these authors makes it possible to take into account the effect of the deformations of the solid skeleton, but is probably not the most appropriate to studying in detail the viscous and thermal losses [8]. Numerical homogenization methods performed on an appropriate structure (C), such as Kelvin or Weaire-Phelan structures, encapsulate both realistic (the model and the geometry of the foam are quantitatively comparable) and parametrizable salient features of the real microstructure, allowing modifications of cellular morphology to be accounted for across the scales. This builds up an appropriate framework for discussion with chemists. At the present time, however, no optimal morphological configuration of cellular foams has been manufactured to maximize sound absorption and/or sound transmission loss for a given frequency range.

Within the above context, this study aims at (i) exploring whether milli-fluidic techniques [6] can be used to tune the membrane content of cellular foams (and therefore, the transport and sound absorbing properties of these materials); (ii) assessing the effects of the membrane content on the sound absorbing and underlying visco-thermal properties; (iii) developing a model to predict the evolution of these macroscopic properties as a function of the membrane content. This model will be compared to other formulations proposed elsewhere in the literature, such as the Doutres et al. (DAD) model [20,21] (which accounts for the fraction of fully open/fully closed windows) and the Hoang and Perrot (HP) model, which is based on a homogeneous degree of opening of membranes [23,24].

This paper is organized as follows. In Section 2.1, we present a simple but efficient fabrication route for obtaining low-density monodispersed polymeric foams with a tuned membrane content at constant porosity. The membrane distribution and acoustical properties of the foams thus produced are then studied using optical photomicrography and airflow resistivity, combined with three-microphone standing wave tube measurements. In order to analyze the relationship between the membrane distribution and sound absorbing properties, a three-dimensional regular unit cell model is subsequently proposed. A comparison between the experimental values and the numerical predictions is finally provided for relevant quantities of interest.

2. Membrane-induced effect on sound absorption: experimental evidence

In this section, we detail experiments conducted on real solid foams. In particular, the foaming process, the microstructural characterization and the measurements of normal incidence sound absorption and of the macroscopic parameters are presented.

2.1. Fabrication of controlled polymer foams

We fabricate solid polymer foam samples having fixed values for both gas volume fraction and monodisperse bubble diameter D_b, but a tunable membrane content. The experimental procedure can be described as follows (see Fig. 1):

(1) A monodisperse precursor aqueous foam is generated. Foaming liquid, i.e., TTAB (Tetradecyl Trimethyl Ammonium Bromide) at 3 g/L in water, and nitrogen are pushed through a T-junction allowing bubble size control by adjusting the flow rate of each fluid. The bubbles produced are collected in a glass column and a constant gas fraction over the foam column is set at 0.99 by imbibition from the top with foaming solution [25].
(2) An aqueous gelatin solution is prepared at a mass concentration C_{gel} within the range 12–18%. As it will be shown in the following, low (respectively high) gelatin concentrations lead to the smaller (respectively larger) membrane contents. For the present study we have taken advantage of this effect for tuning the membrane content. Note that the opening process occurring during the drying stage is complex and it has not been studied so far. The temperature of this solution is maintained at $T \approx 60\,^{\circ}$C in order to remain above the sol/gel transition ($T_{(s/g)} \approx 30\,^{\circ}$C).
(3) The precursor foam and the hot gelatin solution are mixed in a continuous process thanks to a mixing device based on flow-focusing method [26]. By tuning the flow rates of both the foam and the solution during the mixing step, the gas volume fraction can be set, $\phi_0 = 0.8$. Note also that the bubble size is conserved during the mixing step. The resulting foamy gelatin is continuously poured into a cylindrical cell (diameter: 40 mm; height: 40 mm) which is rotating around its axis of symmetry at approximately 50 rpm. This process allows

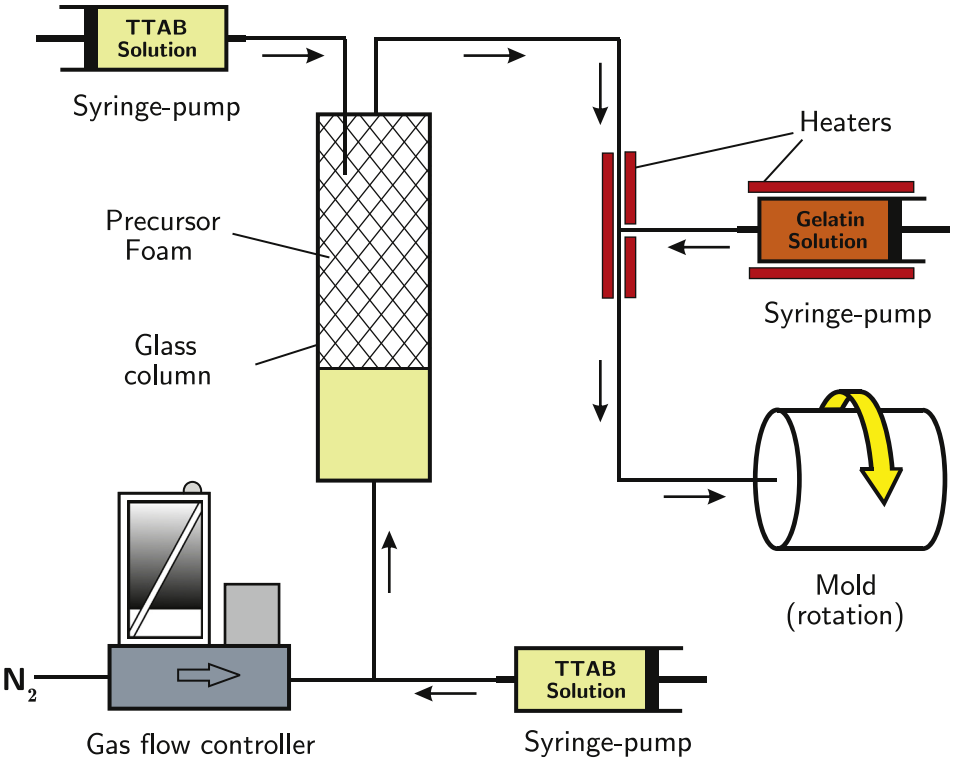

Fig. 1. Schematic description of the foaming process.

for gravity effects to be compensated until the temperature decreases below $T_{(s/g)}$.

(4) The cell is left at rest during one hour, at 5 °C, and is then placed in a climatic chamber ($T = 20$ °C and RH = 30%) for a week. During this stage, water evaporates from the samples and the gas volume fraction increases significantly.

(5) After unmolding, a slice (thickness: 20 mm; diameter: 40 mm) is cut. The slice is used to perform acoustical measurements, while the cut extremities are used for microstructural characterizations [22] (i.e., the peripheral surface is used to measure the pore size [27]).

2.2. Characterization of the foam samples

2.2.1. Pore volume fraction

As the specific gravity of dried gelatin was measured to be 1.36, volume and weight measurements of the dried foam samples allow the pore volume fraction to be determined. For the gelatin concentrations used in this study, the pore volume fraction was found to vary between 0.977 and 0.983. Subsequently, this parameter was considered constant and equal to 0.980 ± 0.003.

2.2.2. Pore size

Through a preliminary calibration, the observation of the sample surface (see Fig. 2a) allows for the pore (bubble) size to be measured. The calibration procedure can be described as follows. Bubbles collected in the glass column (precursor in the Fig. 1) were first sampled and squeezed between two glass plates separated by 100 μm. The surface was next measured and using volume conservation, the bubble gas volume and mean bubble diameter D_b were determined (with a precision of 3%). Moreover, the mean length L_p characterizing the Plateau borders of the precursor foam at the column wall was measured. It is found that $D_b = (1.68 \pm 0.06)L_p$, with $D_b = 810 \pm 30$ μm for all samples. This relation can be used to estimate the pore size in the dried gelatin samples.

In addition, the degree of anisotropy was assessed by controlling the value of the ratio D_{b1}/D_{b2} (see Fig. 2b). Note that anisotropy was also considered in both the axial and radial directions. In practice, this ratio is typically smaller than 1.15 for all samples, so that the effect of geometric anisotropy will be neglected from now on.

2.2.3. Cell window characteristics

In this work, cell windows have been characterized by observing the top and bottom surfaces of samples through a microscope (see Fig. 2). By scanning sample surface and focusing on individual windows, we position in each window a polygon by making its edges coincide with the Plateau borders (Fig. 2c). Then, the polygon area, the number of edges and their lengths L are characterized.

In terms of cellular morphology properties, the distribution of the number of edges per face shown in Fig. 3c is in close agreement with previous experimental [28] and numerical [29] studies. The measured morphological properties, such as the edge length and face area distributions shown in Fig. 3a–b, are very close to results shown in Ref. [29] for foams with a monodispersed or relaxed structure. The periodic unit cell modeling is based on a Kelvin cell and is described in Section 3.1. The locations of the distribution peaks observed in Fig. 3a–b are close to the ones obtained in a Kevin cell for which $L/\sqrt[3]{V_{ce}} \approx 0.45$ (with $V_{ce} = D_b^3/2$, the volume of the Kelvin cell) and $A_k/\sqrt[3]{V_{ce}^2} \approx 0.38$ (with $A_k = (6 \times L^2 + 8 \times 3\sqrt{3}/2L^2)/14$). In addition, as shown in Fig. 3c, the main proportion of 5-sided faces in all samples is consistent with the averaged number of edges of the cellular model $(4 \times 6 + 8 \times 6)/14 \approx 5.14$ (the average being taken over all the faces of the Kelvin cell).

The membrane content is evaluated by measuring the closure ratio of windows separating the pores, using the following procedure. Over several hundred windows observed on both the top and bottom sample surfaces, the proportion of fully closed windows x_c is

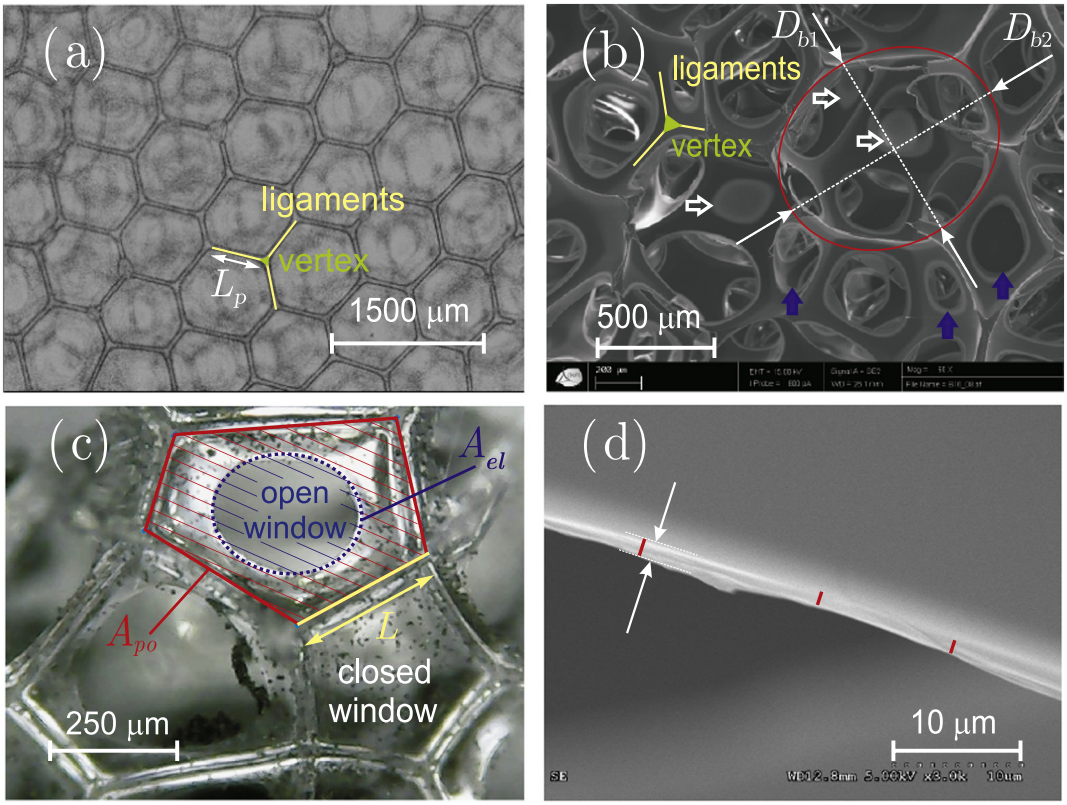

Fig. 2. Characterizations of dried-gelatin foam materials: top view of foam sample (a), degree of anisotropy (b), membrane closure ratio (c), and membrane thickness (d).

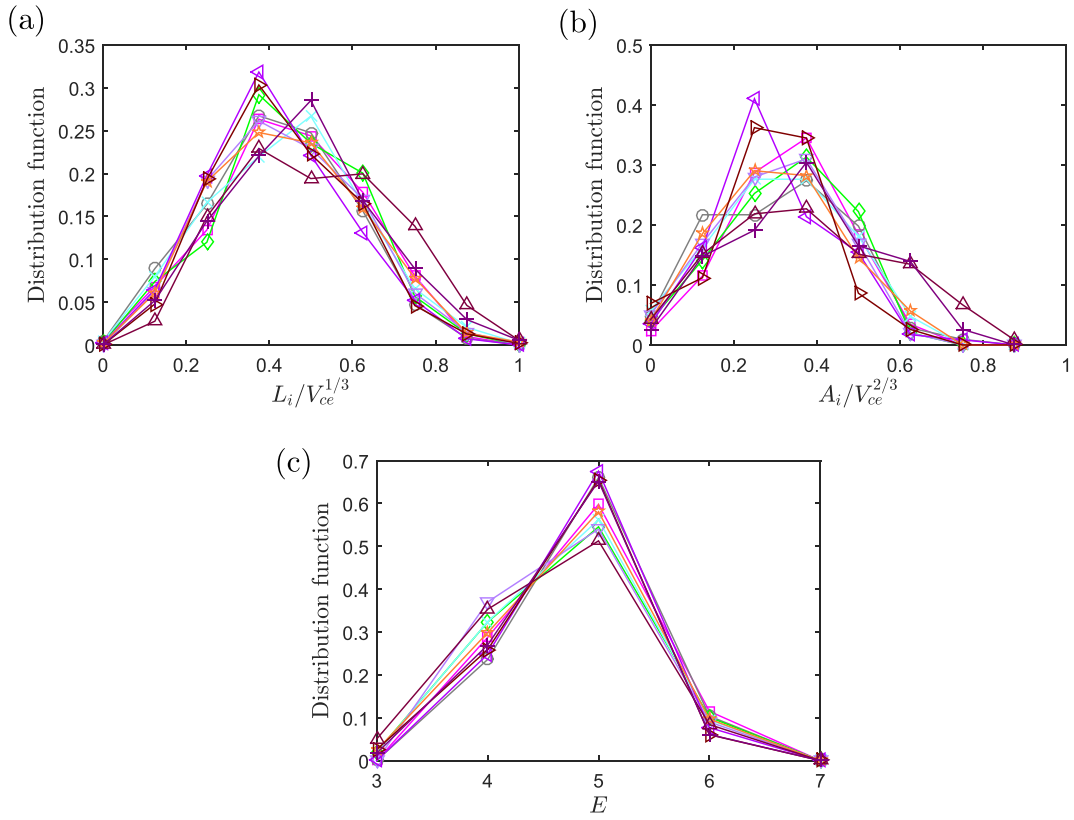

Fig. 3. Morphological properties measured on foam samples for S1(□), S2(○), S3(◇), S4(×), S5(▽), S6(◁), S7(★), S8(▷), S9(△), and S10(+). The results are shown for the normalized edge length distributions (a), the normalized face area distributions (b), and the distributions of faces with E edges (c). The integral of each distribution is normalized to unity.

measured. Therefore, the proportion of open windows, denoted by x_o, is $x_o = 1 - x_c$. For each window, the closure ratio of membrane r_c is also measured: $r_c = 1 - \sqrt{A_{el}/A_{po}}$, where A_{po} is the window area (the area of the corresponding polygonal face) and A_{el} is the aperture area (the area of the fitting ellipse with the aperture, see Fig. 2c). The average of the closure ratio $\langle r_c \rangle$ is then calculated. In the following, a distinction will be made between the mean closure ratio $\langle r_{c,c} \rangle$ of closed windows (equal to one) and the mean for open windows, denoted by $\langle r_{c,o} \rangle$. The three mean closure ratios are related by the following equation: $\langle r_c \rangle = x_c + x_o \times \langle r_{c,o} \rangle$. Note that in order to get all the structural information required for the PUC modeling, this treatment is refined by separating the "square-like" windows having 4 or less edges (referred to as '*sq*'), from the "hexagon-like" windows having more than 4 edges (referred to as '*he*').

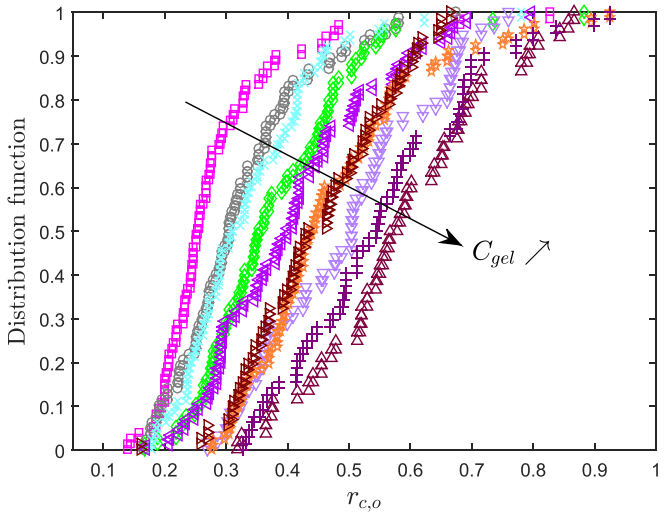

Fig. 4. Distribution function of the window closure ratio measured on foam samples. The results are shown for: S1(□), S2(○), S3(◇), S4(×), S5(▽), S6(◁), S7(★), S8(▷), S9(△), and S10(+).

The structural characterization is completed by a measurement of the membrane thickness through SEM images (Fig. 2d). From ten micrographs, the average thickness was measured to be equal to $1.5 \pm 0.25\,\mu m$, which is close to thicknesses measured for similar polymer foams [22,24].

Fig. 4 shows the cumulative distribution function of window closure ratio for each sample, and Table 1 gives the corresponding mean value $\langle r_{c,o} \rangle$ and proportion of closed windows x_c. The gelatin concentration C_{gel} (varying from 12% to 18%) in the foaming solution appears as a control parameter to tune the membrane content of foam windows. It appears that samples prepared with the same gelatin concentration may result in different mean closure ratios after drying. The mapping between the fabrication parameters and the cellular morphology parameters is given through an experimental design.

It is worth mentioning that the closure ratio of membranes for the larger windows tends to be slightly smaller than the one for the smaller windows, for all foam samples: $r_c^{he} \leqslant r_c^{sq}$ (the big windows are more likely to rupture than small ones). One may however simplify this feature by considering, on average, that all the open windows of the PUC have the same closure ratio, given by $\langle r_{c,o} \rangle = (r_c^{sq} x_o^{sq} + r_c^{he} x_o^{he})/(x_o^{sq} + x_o^{he})$. As shown in Table 1, such a statistical approach leads to a firm trend in which the level of closure ratio $\langle r_{c,o} \rangle$ increases with the increasing proportion of fully closed windows x_c, which leads to an increase of membrane content $\langle r_c \rangle$ from foam S1 to foam S10.

Table 1
Microstructural characteristics of foam samples.

Sample	S1	S2	S3	S4	S5	S6	S7	S8	S9	S10
C_{gel} (%)	12	13	16	16	16	17	18	18	18	18
x_c (%)	7.1	16.7	21.0	30.7	40.4	46.3	50.8	68.8	77.9	86.2
$\langle r_c \rangle$	0.33	0.44	0.47	0.60	0.65	0.73	0.74	0.83	0.91	0.94
$\langle r_{c,o} \rangle$	0.28	0.32	0.33	0.38	0.41	0.50	0.47	0.45	0.58	0.55
x_o^{sq} (%)	20.8	18.4	15	12.7	10.4	8.2	6.6	6.1	6.3	3.4
x_c^{sq} (%)	4.2	8.1	12.4	16.1	19.8	23.6	22.1	17.9	18.2	24.9
x_o^{he} (%)	72.1	64.9	64	56.6	49.2	45.5	42.6	26.1	15.8	11.2
x_c^{he} (%)	2.9	8.6	8.6	14.6	20.6	22.7	28.7	50.9	59.7	61.3

2.3. Acoustic measurements

We determined the macroscopic parameters by acoustic measurements performed in a three-microphone impedance tube (length: 1 m, diameter: 40 mm); see Ref. [30] and references therein. The test frequency ranges from 4 Hz to 4500 Hz with a step size of 4 Hz. Note that the three-microphone impedance tube method consists in measuring the pressure transfer functions, H_{12} and H_{13}, between the microphones (see Fig. 5). The sound absorbing coefficient at normal incidence SAC_{NI} is estimated as $SAC_{NI} = 1 - |p^-/p^+|^2$, in which, p^- and p^+ are respectively the pressure created by the outgoing and the ingoing waves at the surface of the sample. Based on these measured data, Panneton and Olny [12,13] proposed an inverse characterization method to estimate the transport properties of porous materials. This characterization method requires the porosity and the static viscous permeability k_0 as input parameters using the approximate but robust JCAL semi-phenomenological model [8,9,11]

Samples showing high permeability, i.e., $k_0 > 10^{-9}\text{m}^2$, were characterized by a direct measurement of the pressure drop ΔP_{sp} as a function of the volumetric air flow rate Q. This was achieved within steady state conditions in a Darcy flow regime ($\text{Re}_{D_b} = V_o D_b \rho/\eta < 1$, where η is the dynamic viscosity of the fluid), as specified in the standard ISO 9053:1991. The Darcy permeability was then determined as follows:

$$k_0 = \eta Q H_{sp}/A\Delta P_{sp} \quad , \tag{1}$$

with the thickness of sample $H_{sp} \approx 20$ mm and the circular cross-sectional area $A \approx 12.57\,\text{cm}^2$. More precisely, the permeability of each sample was measured for various static airflows ranging from 350 to 70 cm^3/s (with incremental reductions) and determined by interpolation for a linear airflow velocity of 0.5 mm/s. The relative error of this measure is lower than 10%. The static viscous permeability value k_0 can also be determined as the imaginary part of the low frequency behavior of the effective density $\tilde{\rho}$ [12]: $k_0 = -\eta/\lim_{\omega\to 0}[\Im(\omega\tilde{\rho})]$, where ω is the angular frequency. Using this method, the air permeability is determined asymptotically based on the frequency range [80–800] Hz. Because the fluid saturating the porous medium is generally air in the context of sound absorbing materials, any contribution to viscosity due to the nature of the fluid can be excluded. Then, the use of the airflow resistivity $\sigma = \eta/k_0$ (Nsm^{-4}) is preferred to that of the static viscous permeability k_0 (m^2). For foams having a significant fraction of closed windows, the inverse method just described above [12,13] used to characterize the transport parameters fails to determine the parameters governing the thermal effects, i.e., the thermal characteristic length Λ' [11] and the static thermal permeability k_0' [9].

2.4. Experimental results and discussion

Fig. 6 illustrates the evolution of the sound absorbing coefficient at normal incidence as a function of the membrane content $\langle r_c \rangle$.

As the membrane content increases, the sound absorption coefficients display a transition from the most open pores (S1, $\langle r_c \rangle = 0.33$) to the least open ones (S10, $\langle r_c \rangle = 0.94$). This analysis shows that the highest sound absorbing values (at constant thickness, 20 mm) arise for intermediate situations (S6, $\langle r_c \rangle = 0.73$). For $\langle r_c \rangle = 0.73$, visco-thermal losses are produced such that $SAC_{NI} \sim 100\%$ absorption peak can be obtained at ~1600 Hz. The sound absorption increases monotonically when r_c increases for $\langle r_c \rangle < 0.73$ and then decreases monotonically when $\langle r_c \rangle$ continues to increase above the critical value $\langle r_c \rangle = 0.73$. At low membrane contents, most of the pores are fully open: consequently, the sound waves can propagate through the foam without strong losses, and be reflected on the rigid backing. On the other hand, at high membrane contents, the sound waves can hardly penetrate into the cellular foam and most of their energy is reflected instead of being transmitted and absorbed by the porous structure.

Because most of the sound absorbing behavior of porous media can be derived from analytic semi-phenomenological [8,9] models once estimates of transport parameters are obtained, a further analysis of the measured transport coefficients of the porous samples under study is clearly necessary. The following remarks can be made regarding the transport parameters (see Table 2 and Fig. 12).

- Because membranes obstruct some windows, increasing $\langle r_c \rangle$ reduces the mean aperture size and thus, increases the static airflow resistivity σ. As well as affecting the flow resistivity, the

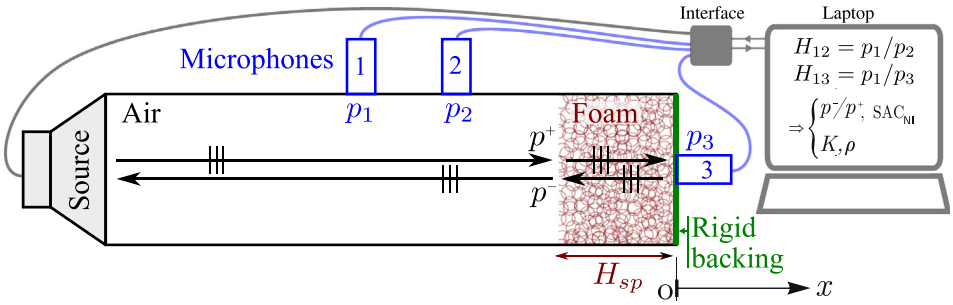

Fig. 5. Experimental setup of the three-microphone impedance tube method.

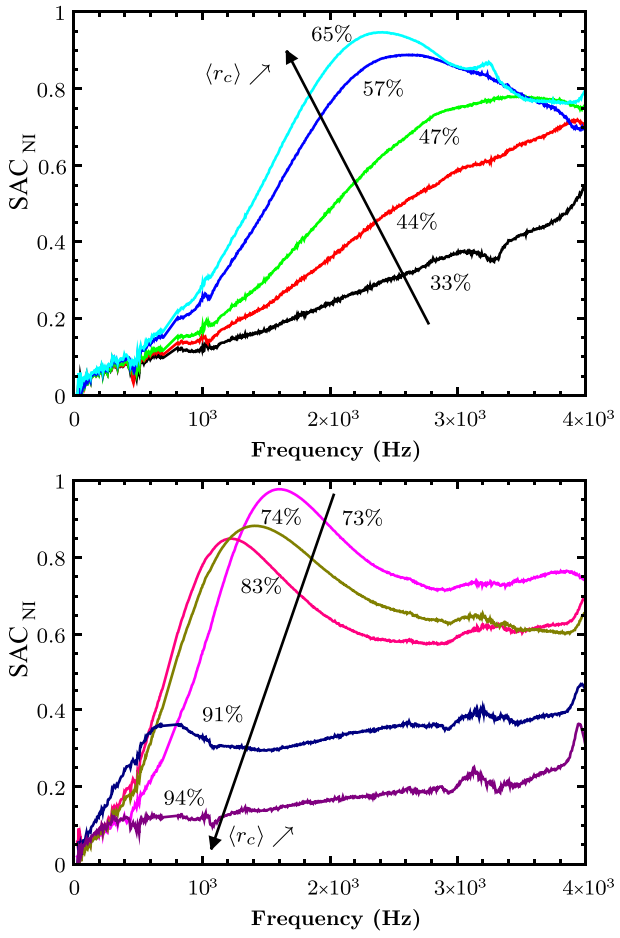

Fig. 6. Effect of the mean closure ratio on the sound absorbing coefficient at normal incidence with a sample thickness of 20 mm and a rigid backing.

membrane closure ratio has an important effect on tortuosity. Membrane closure ratio, in turn, increases the fluid path length and therefore, the tortuosity α_∞. The increase in tortuosity with closure ratio accounts for the lowering of the frequency of the quarter wavelength resonance shown in Fig. 6.

- Similarly, closing some windows or reducing the aperture size of open windows, reduces the values of the viscous characteristic length Λ, since Λ is defined as a pore-volume-to-surface ratio in which a weighting procedure [Eq. (7)] substantially favors the smaller apertures. Note that the values of Λ/D_b are close to the mean aperture radius $\langle R_o \rangle$, calculated by including the closed windows for which $R_o = 0$ (Fig. 12a).
- The ratio Λ'/Λ is close to 2 for small values of $\langle r_c \rangle$ (as observed in fibrous materials; see for instance Appendix 5.C of Ref. [7]). However, it turns out that Λ'/Λ should increase significantly as $\langle r_c \rangle \to 1$ since in the meantime $\Lambda \to 0$ [and $\Lambda' \to \Lambda'_{fc}$, see Eq. (18)].
- Furthermore, we note that the formal inequality $k'_0 \geq k_0$ [31] is verified experimentally, and that k'_0/k_0 also diverges when $\langle r_c \rangle \to 1$ as $k_0 \to 0$ as shown in Fig. 12. At constant pore size D_b, k'_0 decreases slowly with increasing membrane content (fluid-structure interface) whereas k_0 decreases strongly with membrane content (fluid obstruction).

3. Distinction between aperture size and fraction of closed windows: numerical simulations

3.1. Unit cell modeling approach

The space-filling arrangement of Kelvin's cell is a good representative structure for real cellular foams with equal-sized bubbles or cells of equal volume [32]. The idealized Kelvin's tetrakaidecahedron is widely used for modeling foams having high porosity[27]. The cell is a 14-sided polyhedron with 6 square and 8 hexagonal faces. In order to use this cell to study cellular materials, the cross sections of the struts of this framework might be modeled using different shapes; such as circular, triangular or concave triangular. Interestingly, the ligament shape has relatively limited influence on the macroscopic acoustic properties [20,33], so that the strut can be treated using simple shapes (e.g., triangular tubes with a constant cross section). Thus, the cell skeleton is made of idealized ligaments having a length L, and an equilateral triangular cross-section of edge side r (see the Appendix A). Fig. 7a shows the periodic unit cell used to represent the local structure of the foam samples. The corresponding finite-element mesh is shown in Fig. 7b. Note that all hexagonal windows and three square windows are located in the cube and that six square windows (half counted as they are shared by cells outside the cube) belong to the faces of the cube. Due to the periodicity, the square windows within the opposite cube faces are linked, i.e. both are either closed or open at the same time.

In this work, the boundary value problems (BVPs) governing visco-thermal loss mechanisms are solved by using the finite element method (at convergence, the mesh contains 207, 361 tetrahedral elements, see Fig. 7b). A commercial code, Comsol Multiphysics v5.2, was used. As we are interested in membrane induced-effects on the transport and sound absorbing properties, we partially or totally close the windows by adding rigid membranes with a thickness of 2 μm. The latter membranes constitute a rigid geometric barrier of negligible thickness. The macroscopic linear elastic properties of three-dimensional periodic unit cell models have also been computed elsewhere by taking into account the properties of the base material (e.g., Young's modulus and Poisson's ratio) [23,34], and a strong contribution of the membrane thickness was found. Investigating the role of linear elastic properties of the base material and membrane thickness in more detail in the full three-dimensional finite-element model considered here is more difficult because one can no longer use the symmetry properties of a regular periodic unit

Table 2
Transport parameters of the fabricated foam samples.

Sample	S1	S2	S3	S4	S5	S6	S7	S8	S9	S10
Mean closure ratio, $\langle r_c \rangle$	0.33	0.44	0.47	0.60	0.65	0.73	0.74	0.83	0.91	0.94
Mean aperture radius, $\langle R_o \rangle$(μm)	161	136	125	105	81	64	62	34	25	21
σ (kN s m^{-4}) direct meas.	1.7	3.0	4.0	7.0	10.6	Out of range				
σ (kN s m^{-4}) acoustic meas.	1.7	4.6	5.1	10.5	8.7	22.8	37.3	41.4	185	1360
$\alpha_\infty(-)$	1.06	1.4	1.69	2.4	2.4	3.78	4.5	5.9	–	–
Λ (μm)	224	165	179	103	95	51	44	67	–	–
k'_0 ($\times 10^{-10}$m^2)	170	190	170	–	130	–	–	–	–	–
Λ' (μm)	490	665	420	–	400	–	–	–	–	–

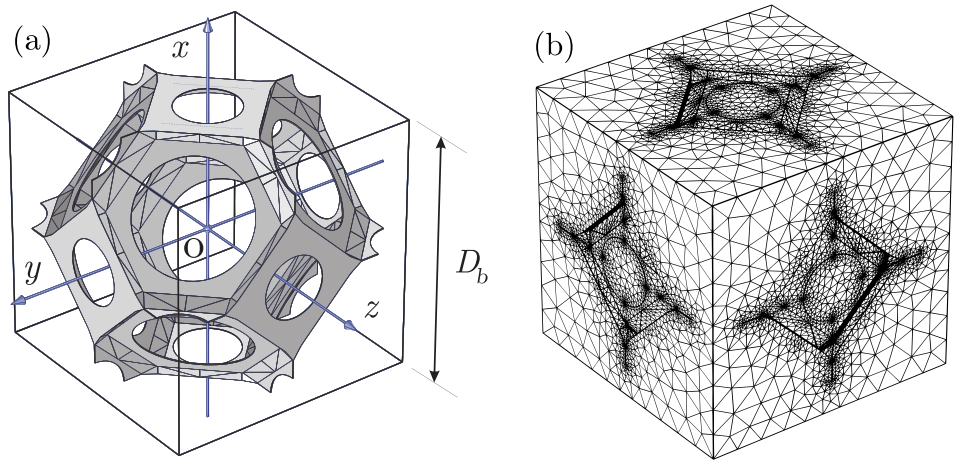

Fig. 7. PUC: skeleton geometry (a) and pore-space mesh (b).

cell which reduces significantly the number of elastic constants to be identified numerically. In the case of an open window, the hole in the membrane is circular. As we attempt to make a numerical reconstruction of real foams, the number of closed windows and the size of the window aperture in the PUC are based on the microstructural characterization of the real samples. The global closure ratio of the cell can be tuned by varying the number of partially closed windows. Therefore, the number of closed hexagons and closed squares per cell are determined by the following equations: $N_o^{sq} = \lfloor 6 \times x_o^{sq} / \left(x_o^{sq} + x_c^{sq}\right) \rceil$ and $N_o^{he} = \lfloor 8 \times x_o^{he} / \left(x_o^{he} + x_c^{he}\right) \rceil$ where $\lfloor \cdot \rceil$ denotes the nearest integer (round) function. The number of fully closed windows is then equal to $N_c^{sq} = 6 - N_o^{sq}$ and $N_c^{he} = 8 - N_o^{he}$. The aperture radius of windows is chosen in accordance with the characterized closure ratio $R_o = (A_{po}/\pi)^{0.5} \times (1 - r_{c,o})$, with $A_{po} = 3\sqrt{3}D_b^2/16$ for hexagonal windows and $D_b^2/8$ for square windows.

Thus, a reconstructed PUC involves N_c^{sq} fully closed squares and N_c^{he} fully closed hexagons. However, different spatial distributions of fully closed windows are possible (except in the simplest cases, e.g., fully open or fully closed cell). The total number of possible configurations $\mathcal{N}_t$ is given by the product of two binomial coefficients (see Fig. 8 for one configuration of each PUC):

$$\mathcal{N}_t = \binom{6}{N_c^{sq}} \times \binom{8}{N_c^{he}}. \tag{2}$$

A 2D representation of the Kelvin cell is useful to localize the position of the closed windows (Fig. 9): the windows numbered from 1 to 3 are associated with squares shared between two cells and located at the face of the cube enclosing the PUC, the windows numbered from 4 to 6 are associated with squares located within the cube, and those from 7 to 14 are associated with hexagons located within the cube. For each configuration, it is possible to define an array in which each element is associated with a window in the PUC, and contains "1" if the window is closed or "0" otherwise. Hence, as soon as the numbers of closed hexagonal windows and closed square windows are defined, all possible configurations of PUC can be found by calculating all permutations of 0 and 1 in the array. We show in Fig. 9b an example of different configurations associated with the simple case, $N_c^{sq} = 1$ and $N_c^{he} = 0$. These configurations are also depicted in Fig. 11a(I) in a tabular form, where each line of the table corresponds to a geometrical configuration (Table 3).

Among all the possible configurations associated with the same number of closed windows, some of them have, with respect to the physical problem considered, a similar behavior. A trivial example is obtained by rotating a given configuration around the axis corresponding to the direction of sound propagation (x-axis), for instance. Other transformations (rotations, translations) exploiting the symmetries of the Kelvin cell also preserve the behavior of the cell. We define a set of 13 transformations as shown in Fig. 10. For each transformation, by comparing the original configurations [Fig. 11a(I)] to

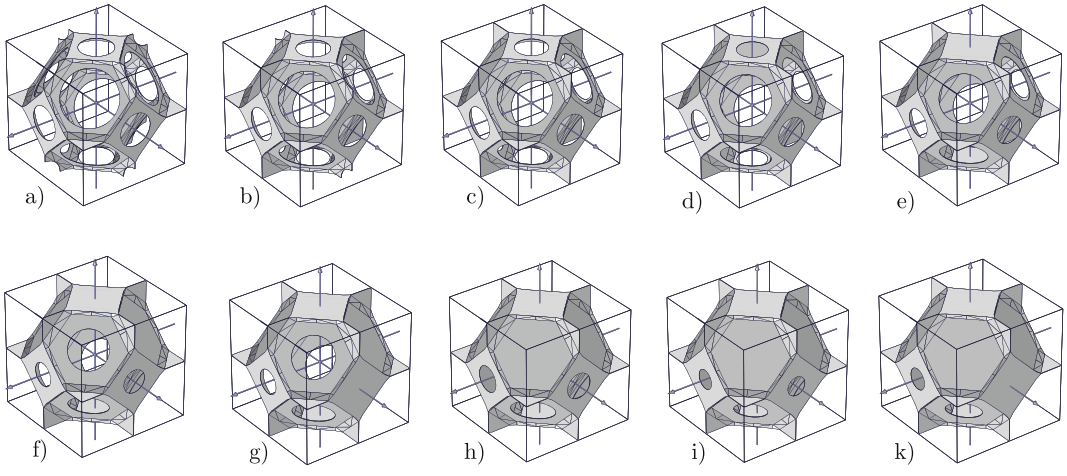

Fig. 8. Illustration of some typical reconstructed PUC corresponding to microstructural characteristics of foam samples S1 to S10. Graphs of the periodic unit cell (a)–(k) corresponding to PUC1–PUC10. Note that, for each PUC, only one configuration among many is depicted.

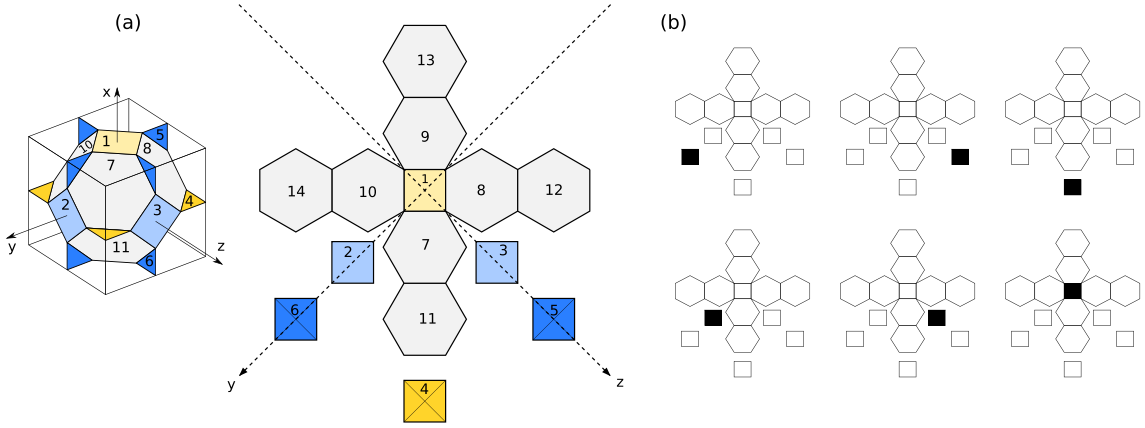

Fig. 9. (a) Reconstruction of a tetrakaidecahedron cell with a 2-dimensional pattern, direction of x axis is perpendicular to faces 1 and 4; (b) the possible configurations associated with PUC1 ($N_c^{sq} = 1$ and $N_c^{he} = 0$).

the transformed configurations [Fig. 11a(II)], we can find the equivalent configurations and associate them together [Fig. 11a(III)]. Then, by considering the results obtained for all transformations, a global calculation of equivalent configurations is performed [Fig. 11a(IV)]; as we show in Appendix B. Thanks to this calculation of equivalent configurations, the number of reference configurations, $\mathcal{N}_r$, we have to compute is drastically reduced compared to the total number of configurations, $\mathcal{N}_t$ (Table 4).

In porous media, pores (or cells in foam) can be disconnected from the percolating pore-network in which fluid flow occurs [35]. In agreement with this result, our PUC simulations predict that, when the number of closed windows is significant, i.e., $N_{sq} \geq 2$ and $N_{he} \geq 4$, no flow through the PUC is possible for several configurations. The number of such closed configurations, $\mathcal{N}_{t,c}$, is given in Table 4. Therefore, the ratio of the total number of open configurations to the total number of configurations, $(\mathcal{N}_t - \mathcal{N}_{t,c})/\mathcal{N}_t$, gives the probability of finding a cell within the percolating pore-space, which is also equal to R_{op}, the ratio of the open porosity ϕ_o to the total porosity ϕ,

$$R_{op} = 1 - \mathcal{N}_{t,c}/\mathcal{N}_t. \tag{3}$$

3.2. Calculations of visco-thermal parameters

3.2.1. Definition of non-acoustic parameters

In this section, we briefly introduce the BVPs that are used for computing the macroscopic properties of the JCAL semi-phenomenological model with 6 input parameters. This semi-phenomenological model relies on two purely geometrical parameters (ϕ, Λ') defined directly from the local geometry of the representative unit cell as $\phi = \int_{\Omega_f} dV / \int_{\Omega} dV$, and $\Lambda' = 2\int_{\Omega} dV / \int_{\partial\Omega} dS$ [11]. Here, Ω is the periodic unit cell and Ω_f denotes the volume of fluid. The 4 remaining transport properties are computed from the solution fields corresponding to three group of PDEs over the unit cell.

Table 3
Definition of the transformations of the original configuration [123456 | 7891011121314].

Symmetry	Shown in	Transformed configuration
Cell permutation	Fig. 10a	[4 5 6 1 2 3|11 12 13 14 7 8 9 10]
Origin point O	Fig. 10b	[1 2 3 4 5 6|13 14 11 12 9 10 7 8]
Rotation 180° around Ox	Fig. 10b	[1 2 3 4 5 6| 9 10 7 8 13 14 11 12]
Rotation 180° around Oy	Fig. 10b	[1 2 3 4 5 6|14 13 12 11 10 9 8 7]
Rotation 180° around Oz	Fig. 10b	[1 2 3 4 5 6|12 11 14 13 8 7 10 9]
Rotation 180° around Oz_1	Fig. 10b	[1 3 2 4 6 5|13 12 11 14 9 8 7 10]
Rotation 180° around Oy_1	Fig. 10b	[1 3 2 4 6 5|11 14 13 12 7 10 9 8]
Rotation 90° around Ox	Fig. 10b	[1 3 2 4 6 5| 8 9 10 7 12 13 14 11]
Reflection in plane Oyz	Fig. 10c	[1 2 3 4 5 6|11 12 13 14 7 8 9 10]
Reflection in plane Oxy	Fig. 10c	[1 2 3 4 5 6|10 9 8 7 14 13 12 11]
Reflection in plane Oxz	Fig. 10c	[1 2 3 4 5 6| 8 7 10 9 12 11 14 13]
Reflection in plane Oxz_1	Fig. 10d	[1 3 2 4 6 5| 9 8 7 10 13 12 11 14]
Reflection in plane Oxy_1	Fig. 10d	[1 3 2 4 6 5| 7 10 9 8 11 14 13 12]

Viscous flow: The low Reynolds number flow of an incompressible Newtonian fluid is governed by the usual Stokes equations in the fluid phase [36,37]:

$$\eta \Delta \mathbf{v} - \nabla \mathrm{p} = -\boldsymbol{G} \quad \text{with} \quad \nabla . \mathbf{v} = 0 \quad \text{in} \quad \Omega_f, \tag{4a}$$

$$\mathbf{v} = 0 \quad \text{on} \quad \partial\Omega, \tag{4b}$$

$$\mathbf{v} \quad \text{and} \quad \mathrm{p} \quad \text{are} \quad \Omega - \text{periodic}, \tag{4c}$$

where $\boldsymbol{G} = \nabla \mathrm{p}^m$ is an imposed macroscopic pressure gradient (a constant unit vector) and ∇p is a microscopic pressure gradient, which is periodic from cell to cell. Symbols $\mathbf{v}$ and p are the velocity and pressure of the fluid, respectively. It can be shown that the non-vanishing components v_x of the local velocity field are given by $v_x = -\mathrm{k}_{0xx} G_x/\eta$. Here, k_{0xx} is a scaled velocity field. Thus, the (scalar) static viscous permeability k_{0xx} is calculated as

$$k_0 = k_{0xx} = \phi \langle \mathrm{k}_{0xx} \rangle, \tag{5}$$

where the symbol $\langle . \rangle$ indicates a spatial average over the fluid-phase.

Inertial flow: In the high frequency limit, the viscous boundary layer becomes negligible and the fluid tends to behave as a perfect one, having no viscosity except in the vicinity of the boundary layer. Consequently, the perfect incompressible fluid formally behaves according to the potential flow problem [8,37]:

$$\nabla . \mathbf{E} = 0 \quad \text{with} \quad \mathbf{E} = -\nabla \varphi + \mathbf{e}, \quad \text{in} \quad \Omega_f, \tag{6a}$$

$$\mathbf{E}.\mathbf{n} = 0, \quad \text{on} \quad \partial\Omega, \tag{6b}$$

$$\varphi \quad \text{is} \quad \Omega - \text{periodic}, \tag{6c}$$

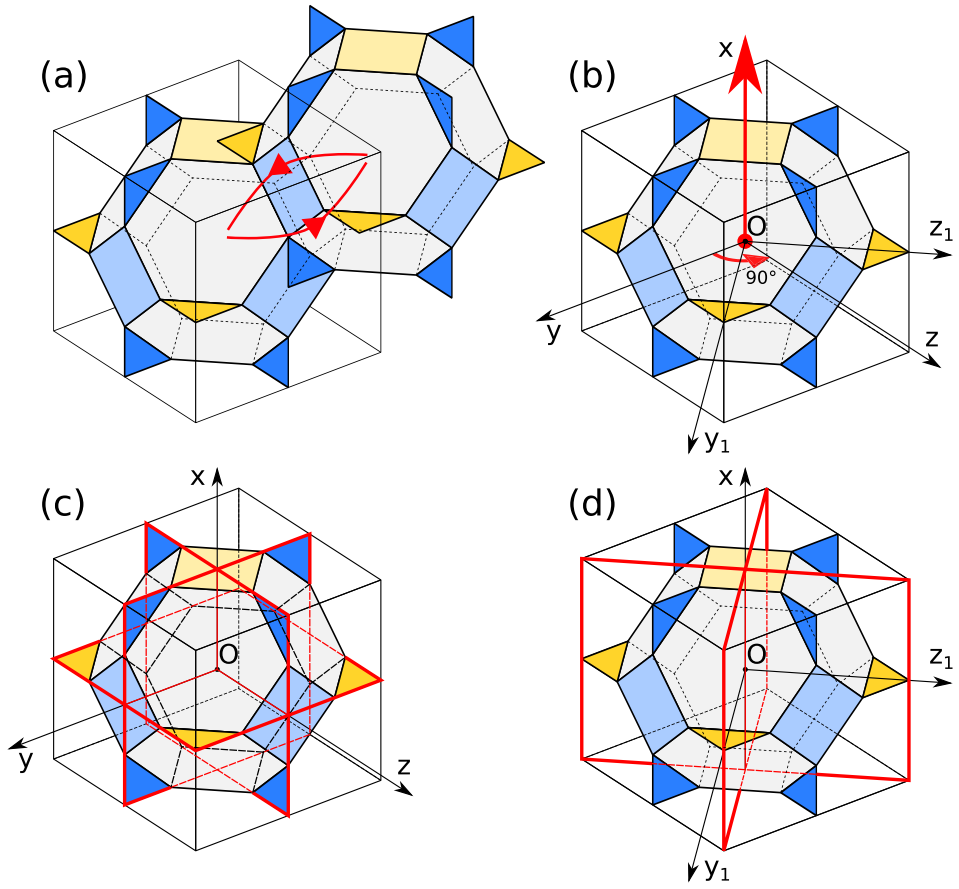

Fig. 10. The symmetry property of the periodic unit cell.

where **e** is a constant unit vector, **E** is the solution of the boundary problem having $-\nabla\varphi$ as a fluctuating part, and **n** is the unit normal to the boundary of the pore region. The viscous characteristic length Λ and the high frequency tortuosity α_∞ are then calculated through

$$\Lambda = \frac{2\int_{\Omega_f}|\mathbf{E}|^2 dV}{\int_{\partial\Omega}|\mathbf{E}|^2 dS} \quad , \alpha_\infty = \frac{\langle|\mathbf{E}|^2\rangle}{\langle|\mathbf{E}|\rangle^2}. \tag{7}$$

Thermal effect: Under the excitation of an external harmonic source with angular frequency ω, in a pore having a cross-section with dimensions much smaller than the wavelength, the pressure is uniform over the cross section (uniform and steady source term). This constancy follows from a simple two-scale analysis. A proof is given in Appendix A of Ref. [9]. To the lowest order, the excess temperature field then originates from a spatially uniform, harmonic, heating in the air domain, with perfect absorbing conditions on the solid boundaries. This problem was investigated by Rubinstein and Torquato [38] using the method of homogenization. The static thermal permeability is given by:

$$k_0' = \langle u\rangle, \tag{8}$$

where the scaled temperature field u solves the canonical equations,

$$\Delta u = -1, \qquad \text{in} \qquad \Omega_f, \tag{9a}$$

$$u = 0, \qquad \text{on} \qquad \partial\Omega. \tag{9b}$$

It is worthwhile noticing that Δu is dimensionless. Therefore, u and k_0' have the dimension of a surface.

3.2.2. Calculation of the average of non-acoustic parameters

For the purpose of the calculation of non-acoustic properties, the configuration of each unit cell is considered based on the spatial distribution of the fully closed faces. Of course, this distribution has no influence on the geometric parameters (i.e., the thermal characteristic length Λ' and the porosity ϕ, for PUCs without a closed pore-space).

In order to compute the effective macroscopic transport parameters, for each unit cell of foam sample, let us first introduce two averaging operators:

$$\langle\cdot\rangle_V = \frac{1}{V_f}\int_{\Omega_f} .dV \quad , \tag{10a}$$

$$\langle g_j\rangle_{\mathcal{N}} = \frac{1}{\mathcal{N}_t}\sum_{j=1}^{\mathcal{N}_t} g_j = \frac{1}{\mathcal{N}_t}\sum_{k=1}^{\mathcal{N}_r} n_k g_k, \tag{10b}$$

in which n_k is the number of equivalent configurations having the same value g_k. Hence only one representative configuration among n_k is selected to perform the numerical computation. In the total number of possible configurations $\mathcal{N}_t$ for each unit cell in Eq. (2), this involves typically $\mathcal{N}_r$ reference configurations (see Section 3.1). The values of $\mathcal{N}_t$ and $\mathcal{N}_r$ are summarized in Table 4.

Then, the effective static viscous and thermal permeabilities of each foam sample were deduced from the averages of the local permeability fields k_{0xxj} and u_j of each configuration. It follows that:

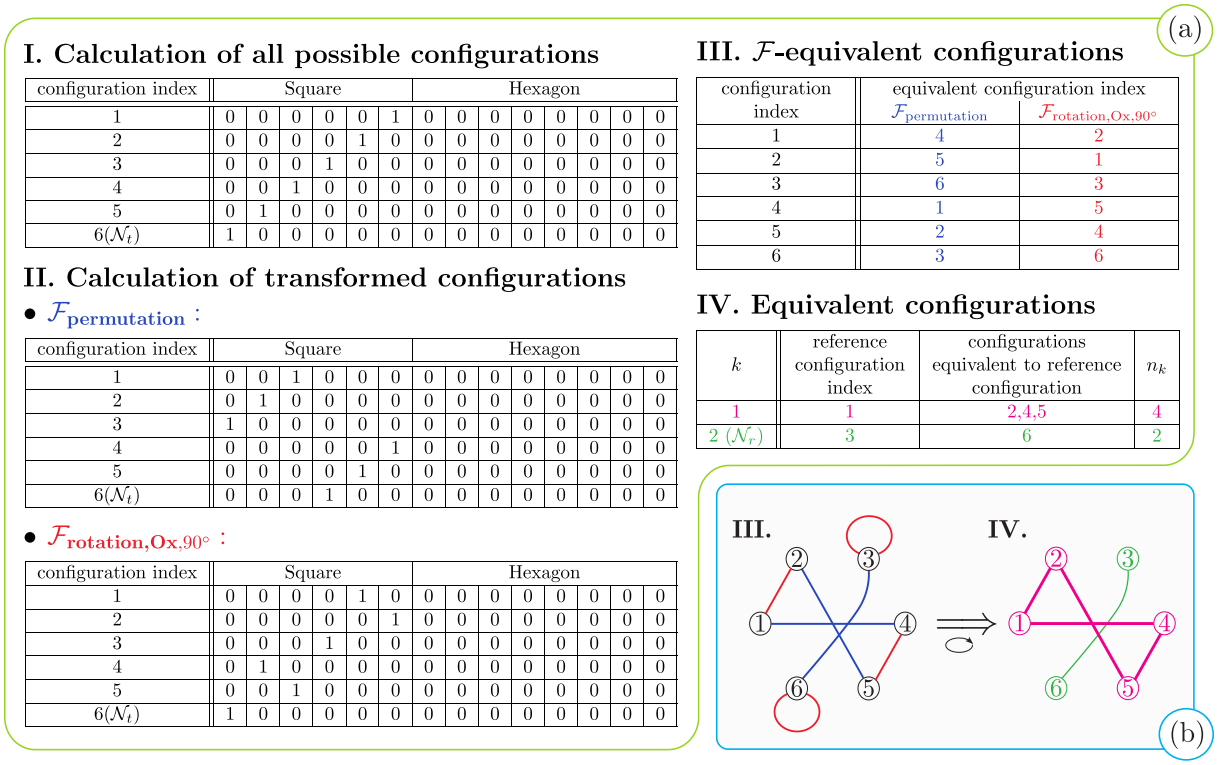

I. Calculation of all possible configurations

configuration index	Square						Hexagon							
1	0	0	0	0	0	1	0	0	0	0	0	0	0	0
2	0	0	0	0	1	0	0	0	0	0	0	0	0	0
3	0	0	0	1	0	0	0	0	0	0	0	0	0	0
4	0	0	1	0	0	0	0	0	0	0	0	0	0	0
5	0	1	0	0	0	0	0	0	0	0	0	0	0	0
6($\mathcal{N}_t$)	1	0	0	0	0	0	0	0	0	0	0	0	0	0

II. Calculation of transformed configurations

• $\mathcal{F}_{\text{permutation}}$:

configuration index	Square						Hexagon							
1	0	0	1	0	0	0	0	0	0	0	0	0	0	0
2	0	1	0	0	0	0	0	0	0	0	0	0	0	0
3	1	0	0	0	0	0	0	0	0	0	0	0	0	0
4	0	0	0	0	0	1	0	0	0	0	0	0	0	0
5	0	0	0	0	1	0	0	0	0	0	0	0	0	0
6($\mathcal{N}_t$)	0	0	0	1	0	0	0	0	0	0	0	0	0	0

• $\mathcal{F}_{\text{rotation,Ox,90°}}$:

configuration index	Square						Hexagon							
1	0	0	0	0	1	0	0	0	0	0	0	0	0	0
2	0	0	0	0	0	1	0	0	0	0	0	0	0	0
3	0	0	0	1	0	0	0	0	0	0	0	0	0	0
4	0	1	0	0	0	0	0	0	0	0	0	0	0	0
5	0	0	1	0	0	0	0	0	0	0	0	0	0	0
6($\mathcal{N}_t$)	1	0	0	0	0	0	0	0	0	0	0	0	0	0

III. $\mathcal{F}$-equivalent configurations

configuration index	equivalent configuration index	
	$\mathcal{F}_{\text{permutation}}$	$\mathcal{F}_{\text{rotation,Ox,90°}}$
1	4	2
2	5	1
3	6	3
4	1	5
5	2	4
6	3	6

IV. Equivalent configurations

k	reference configuration index	configurations equivalent to reference configuration	n_k
1	1	2,4,5	4
2 ($\mathcal{N}_r$)	3	6	2

Fig. 11. (a) Major steps in the equivalent configuration calculation and (b) graphs representing steps III and IV. This figure depicts the simple case where $N_c^{sq} = 1$ and $N_c^{he} = 0$.

$$k_0 = \langle\langle \mathrm{k}_{0xxj}\rangle_V\rangle_{\mathcal{N}_t} \quad , k_0' = \langle\langle u_j\rangle_V\rangle_{\mathcal{N}_t}. \tag{11}$$

Similarly, the effective viscous characteristic length and high frequency tortuosity are obtained from the solution field $\mathbf{E}_j$ for the potential flow problems:

$$\Lambda = \frac{2\left\langle \int_{\Omega_f} |\mathbf{E}|_j^2 dV\right\rangle_{\mathcal{N}}}{\left\langle \int_{\partial\Omega} |\mathbf{E}|_j^2 dS\right\rangle_{\mathcal{N}}} \quad , \alpha_\infty = \frac{\left\langle \langle |\mathbf{E}|_j^2\rangle_V\right\rangle_{\mathcal{N}}}{\left(\langle\langle |\mathbf{E}|_j\rangle_V\rangle_{\mathcal{N}}\right)^2}. \tag{12}$$

Ω_f is the fluid-filled domain, and $\partial\Omega$ is the fluid-solid interface in a unit cell Ω. Details of the above solved local fields are presented in the previous section. Note that because the number of windows is limited in the Kelvin unit-cell, for PUCs with a relatively high number of closed faces (i.e., S8 to S10), some configurations correspond to disconnected fluid flow. This leads us to consider that all the corresponding solution fields are equal to zero.

3.3. Calculations of sound absorbing properties using the JCAL analytical model

The transport parameters k_0, Λ, α_∞ and k_0' presented in Section 3.2 arise in the low- and high-frequency limits of the dynamic frequency-dependent permeability/compressibility. In this section, we describe how these parameters, independent of angular frequency ω, were used to construct simple analytical models (using mathematical principles) described in this section of the visco-inertial [8] and isothermal/adiabatic [9] responses for arbitrary angular frequency ω.

From the macroscopic perspective, the equivalent-fluid approach consists of substituting a rigid porous medium by an effective fluid. This fluid is characterized by an effective density $\tilde{\rho}(\omega)$ [8] and an effective bulk modulus $\tilde{K}(\omega)$ [9,11] as follows [7]:

$$\tilde{\rho}(\omega) = \rho_0\left[\alpha_\infty - j\frac{\phi\sigma}{\omega\rho_0}\sqrt{1 + j\omega\frac{\rho_0}{\eta}\left(\frac{2\eta\alpha_\infty}{\sigma\phi\Lambda}\right)^2}\right], \tag{13}$$

and

$$\tilde{K}(\omega) = \gamma P_0\left[\gamma - (\gamma-1)\left\{1 - j\frac{\phi\eta}{k_0'^2\rho_0 N_{pr}\omega}\sqrt{1 + j\frac{4k_0'^2 N_{pr}\rho_0\omega}{\eta\Lambda'^2\phi^2}}\right\}^{-1}\right]^{-1}. \tag{14}$$

In these equations, σ is the airflow resistivity, ρ_0 and η are the density and dynamic viscosity of the ambient fluid at rest (i.e., air), P_0 the atmospheric pressure, $\gamma = C_p/C_v$ the ratio of heat capacities at constant pressure and volume, N_{pr} the Prantdl number, j the imaginary unit, $\omega = 2\pi f$ the angular frequency.

The wave number $\tilde{k}_c(\omega)$ and the characteristic impedance $\tilde{Z}_c(\omega)$ at normal incidence of a layer of equivalent-fluid backed by an impervious rigid wall are given by [7],

$$\tilde{k}_c(\omega) = \omega\sqrt{\tilde{\rho}(\omega)/\tilde{K}(\omega)}, \qquad \tilde{Z}_c(\omega) = \sqrt{\tilde{\rho}(\omega)\tilde{K}(\omega)} \quad . \tag{15}$$

The sound absorbing coefficient (SAC) at normal incidence (NI) of this porous layer is related to the impedance $\tilde{Z}_s(\omega)$ at the surface $x = -H_{sp}$ of the sample,

$$\mathrm{SAC_{NI}} = 1 - \left|\frac{\tilde{Z}_s(\omega) - Z_0}{\tilde{Z}_s(\omega) + Z_0}\right|^2, \tag{16}$$

with Z_0 is the impedance of the air, and $\tilde{Z}_s(\omega) = -j\frac{\tilde{Z}_c(\omega)}{\phi}\cot[\tilde{k}_c(\omega)H_{sp}]$.

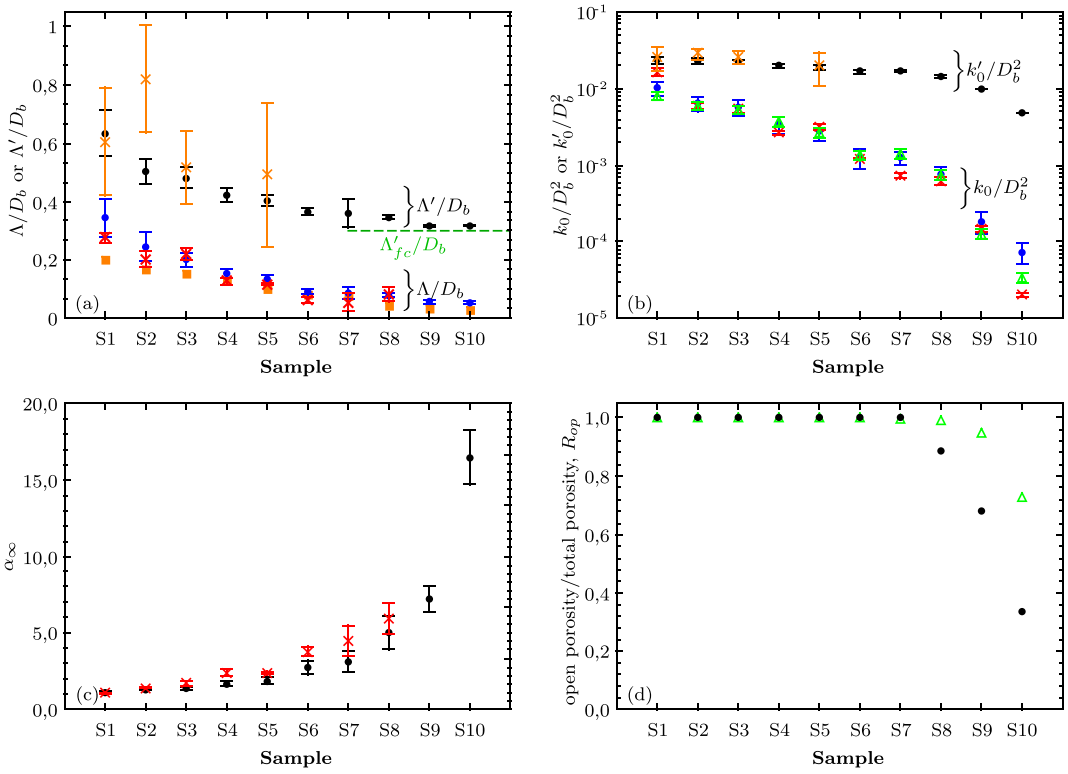

Fig. 12. Dimensionless transport properties for real foam samples (×) and 2-parameter models: PUC computation (○), EM model (△) obtained using the procedure described at the end of Section 4, Eq. (19). The mean aperture radius $\langle R_o \rangle$, calculated by including the closed windows ($R_o = 0$), is added (□) by plotting $\langle R_o/D_b \rangle$ and allows for a comparison with Λ/D_b. Note that the samples S1 to S10 are ordered by increasing mean closure ratios. The error bars on computed values of macroscopic parameters are calculated by considering an error on the characterization of $\langle r_{c,o} \rangle$ equal to ±0.05.

4. Results and discussion

At first, we consider the prediction performance of our "2-parameter" microstructural model (at constant pore size), that requires both the number of closed windows per cell and the size of the window aperture (Section 3.1). Fig. 12 shows that the computed transport parameters compare well to the characterized ones. However, the computed values of tortuosity are lower than the characterized ones. These differences could be due to the limited size of our numerical samples. It is known that in percolating materials [35], the number of cells required for calculations when the fraction of open windows, x_o, is close to the percolation threshold ($1.5/N_v \approx 0.11$, where $N_v = 14$ is the pore neighbor number of the Kelvin structure), should be superior to a few thousands. The fraction of open windows for sample S10, equal to $1 - 0.86 = 0.14$, is very close to the percolation threshold. We can illustrate the limitation of our unit cell modeling by comparing their predicted fraction of open porosity obtained by pore-network calculations performed on large samples in Ref. [35]. As expected, Fig. 12d shows that a modeling approach based on a simple PUC does not accurately predict the open porosity of the real cellular foam samples containing a high fraction of closed windows. We also note that another explanation is possible due to an experimental bias: the microstructural characterization of foam samples was done on the cut extremity of samples, and not on the foam sample used to perform the acoustic measurements. As sample drying occurs by water transfer through the borders of samples, the proportion of open windows in the border could be slightly higher in the extremity than in the bulk of the foam samples.

Thus, it appears clearly that these models taking into account both the proportion of closed window and the closure ratio give quite good estimates of macroscopic parameters. What about the simplest models taking into account one of the two microstructural descriptors? Two "1-parameter" models are considered in the following: (i) the HP model built by considering a fully open foam with a uniform membrane closure ratio tuned in such manner that the computed permeability is equal to the characterized one (it could include closed windows, i.e., square ones) [24], (ii) the DAD semi-empirical model of Doutres et al. which considers the fraction of

Table 4
PUC characteristics corresponding to foam samples S1–S10. In particular, it illustrates the huge discrepancy between the total number of possible configurations $\mathcal{N}_t$ and the reduced number of reference configurations $\mathcal{N}_r$.

Sample	S1	S2	S3	S4	S5	S6	S7	S8	S9	S10
Unit cell	PUC1	PUC2	PUC3	PUC4	PUC5	PUC6	PUC7	PUC8	PUC9	PUC10
N_c^{sq}	1	2	3	3	4	4	5	4	4	5
N_c^{he}	0	1	1	2	2	3	3	5	6	7
$\mathcal{N}_t$	6	120	160	560	420	840	336	840	420	48
$\mathcal{N}_r$	2	6	6	38	36	36	12	36	36	2
$\mathcal{N}_{t,c}$	0	0	0	0	0	0	0	94	135	32

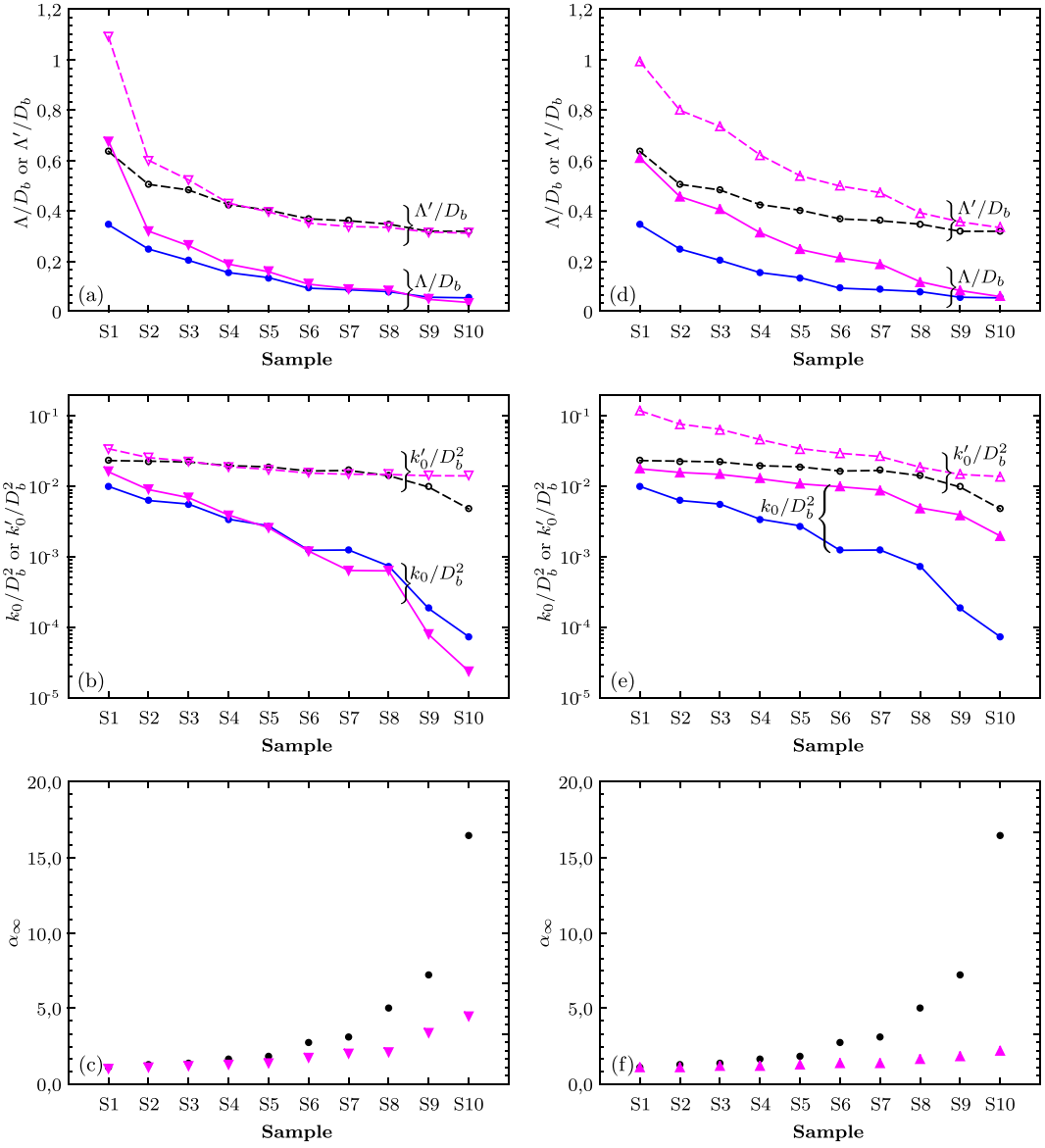

Fig. 13. Comparison of the dimensionless transports predictions obtained for PUC computations and: the HP method (a, b and c), or the DAD method (d, e and f). The results are shown for: PUC computation values (○), HP values (▽), and DAD values (△). Note that the samples S1 to S10 are ordered by increasing mean closure ratio, $\langle r_c \rangle$.

closed windows without taking into account the closure ratio of open windows [20]. Fig. 13 allows the predictions of these "1-parameter" models at constant pore size to be compared with those of the model presented in this paper. Apart from k_0 which is an input parameter taken from experiments, the macroscopic parameter values calculated with the HP model are globally close to our "2-parameter" PUC model. However, the viscous and thermal characteristic length, Λ and Λ', for foams having a low fraction of closed windows (e.g., S1) are not well estimated. For a relatively low mean closure ratio, $\langle r_c \rangle$ (i.e., S1, $\langle r_c \rangle = 0.33$), ignoring the presence of closed windows and considering that the system can be described by membranes at the periphery of open windows instead, could lead to an overestimation of the viscous and thermal characteristic lengths by a factor of two. The DAD model was developed from the standpoint of a cellular morphology which differs significantly from the one studied here, Fig. 13 (right panel). Therefore, it cannot be used to predict the transport parameters of a cellular structure exhibiting both partially open and closed windows in a given proportion. Concerning the SAC predictions of our computational method, Fig. 14 shows that the global trend of experiments is well reproduced by our calculation method. However, a systematic difference between experiments and PUC computations is observed: it is as if the PUC computed curve related to materials having a closure ratio slightly lower than that of the corresponding real foam. The discrepancy could be due to both a systematic error in the PUC calculation (as expected for the porosity, but also for the tortuosity) and/or a bias in the microstructural characterization as described before.

Thus, it appears necessary to take into account both the proportion of open windows x_o and the closure ratio of membrane r_c to get an accurate estimation of macroscopic parameters and sound absorption coefficient. This result is in agreement with the fact that for at least two parameters, the thermal characteristic length Λ' and the static viscous permeability k_0, their physical modelings require us to consider both the fraction of open windows and the window aperture size. Indeed, by considering the idealized geometry of the chosen foam skeleton, the thermal characteristic length, Λ', can be

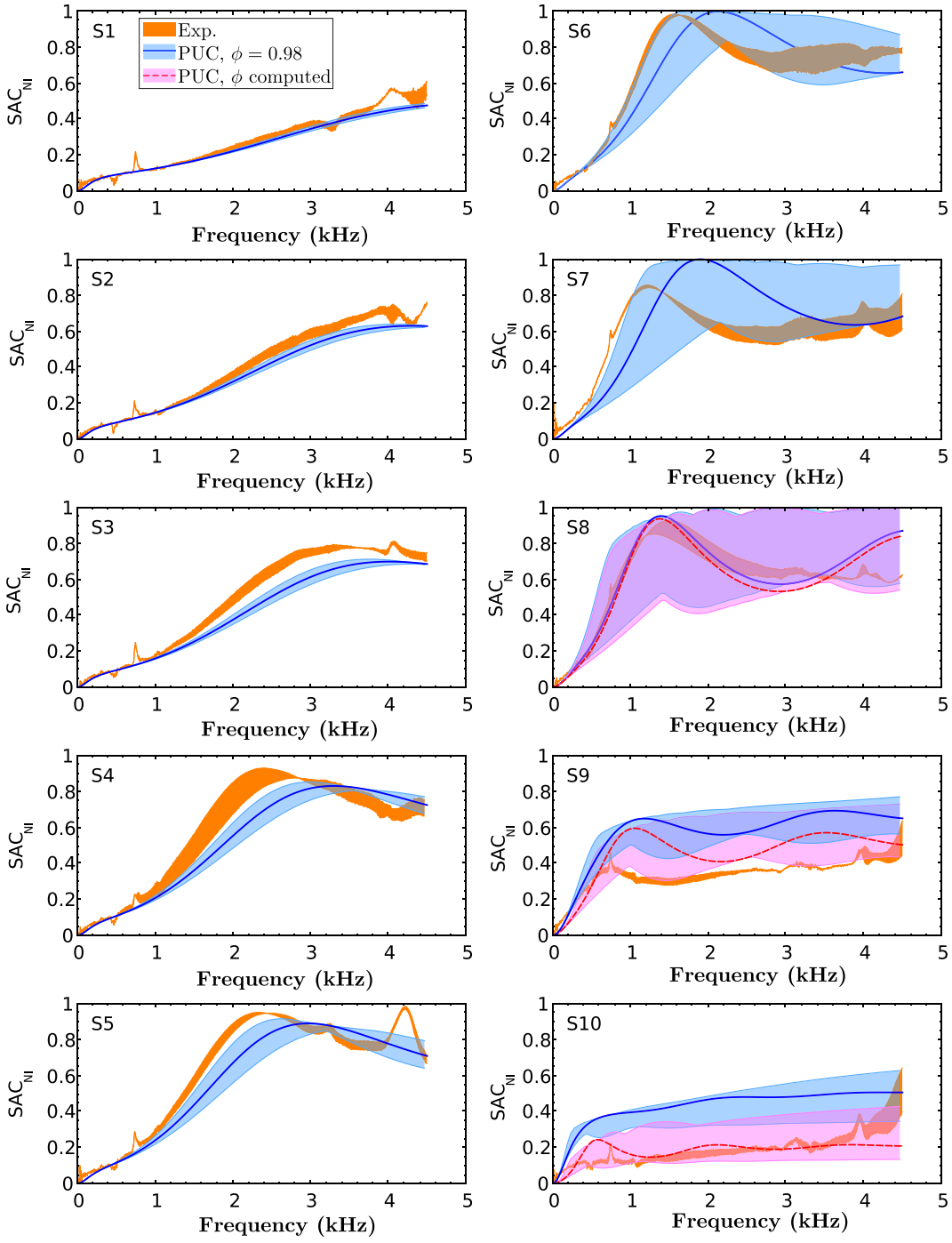

Fig. 14. Sound absorbing coefficients at normal incidence SAC_{NI} of samples, Eq. (16): experiments (orange filled zone), PUC computations with $\phi = 0.98$ (blue filled zone with full line), PUC computations with $\phi = \phi_{o,\text{computed}}$ (red filled zone with dashed line), Eq. (3). The results are shown from top to bottom as: foams S1 to S5 (left panels), and foams S6 to S10 (right panels). The curves are calculated by using the computed macroscopic parameters shown in Fig. 12, and their uncertainties are related to the estimation of errors on macroscopic parameters calculated by considering an error on the characterization of $\langle r_{c,o} \rangle$ equal to ± 0.05. (For interpretation of the references to color in this figure legend, the reader is referred to the web version of this article.)

fully calculated. The detail of the calculation is given in Appendix A for our idealized Kelvin cell. By neglecting a term due to the thickness of membranes, the thermal characteristic length is given by:

$$\frac{D_b}{\Lambda'} = \frac{D_b}{\Lambda'_c} - \frac{N_v}{\phi}\left(\frac{1}{8}x_o^{sq} + \frac{3\sqrt{3}}{16}x_o^{he}\right)(1 - r_c)^2, \tag{17}$$

where Λ'_c is the thermal characteristic length of the fully closed foam.

Eq. (17) shows clearly that the thermal characteristic length Λ' depends on both the proportion of open windows x_o and the closure ratio of membrane r_c.

Alternatively, in the framework of the characterization of partially reticulated foam samples, Λ' can be related to the thermal

characteristic length, Λ'_c, associated with a fully closed foam, as follows:

$$\frac{1}{\Lambda'} = \frac{1}{\Lambda'_c} - \frac{\langle A_o \rangle N_v}{\phi D_b^3}, \tag{18}$$

where $\langle A_o \rangle$ is the mean window aperture area.

The mean window aperture area depends on the aperture window size distribution which can be evaluated from the closure ratio distribution. The value of the thermal characteristic length of a fully closed foam, Λ'_c, appears as the lower bound of the thermal characteristic length, Λ'. For a real foam [27], the ratio volume/surface is close to $D_b/(5.3\sqrt[3]{2})$, leading to $\Lambda'_c/D_b \approx 0.3$.

We consider now the other transport parameter for which a "2-parameter" modeling is required. A model of effective medium (EM) for foam permeability, recently established [35], predicts that the foam permeability, k_0, depends on the amount of closed windows, the membrane aperture size and their proportions. In this model, foam is described as a network of connected pores and the fluid flow through it is governed by a local Darcy law based on the pressure drop at the scale of the membrane aperture. Then, the fluid flow between two connected pores is assumed to be the product of a local permeability and the difference between pore pressures. Moreover, as predicted by the Sampson law, the local permeability depends on the cube of the membrane aperture size. Then, the distribution of membrane aperture radius, $R_{o,i}$, leads to a distribution of local permeability, k_i. Considering the structure of the pore-network and the distribution of local permeability, a mean local permeability k' is calculated by a self-consistent approach. Finally, foam permeability, k_0, is deduced from the mean local permeability. Therefore, the foam permeability can be estimated by the following equations:

$$\frac{2}{N_v k'} = \sum_i \frac{x'_i}{k_i + \left(\frac{N_v}{2} - 1\right) k'}, \tag{19a}$$

$$k_0 = R_{op} \sigma_w k', \tag{19b}$$

where k' denotes the mean local permeability, N_v was defined as the pore neighbor number which is equal to 14 for the Kelvin cell, R_{op} was the value of the open porosity ratio as given by Eq. (3), σ_w is a coefficient depending on the structure of the porous medium and ranging between 3 and 4, $k_i = R_{o,i}^3/3D_b$ is a local permeability associated with an open window having an aperture radius equal to $R_{o,i}$, and x'_i is the fraction of open windows inside the open pore space calculated by including closed windows. The subscript i refers to open windows having the same aperture radius R_i and, therefore, the same local permeability, k_i. Note that the closed windows have a local permeability equal to 0 and a proportion given by $1 - \sum_{i,k_i \neq 0} x'_i$. Eq. (19a) is not an explicit formula, but one can easily evaluate k' by using an iterative solver. Approximate formulae are given in Ref. [35] allowing us to estimate the fraction of open porosity R_{op} and the open window fraction within the open pore-space x'_i by measuring the open window fraction and the average number of neighbor pores. The size of aperture $R_{o,i}$ is calculated from the characterized closure ratios $r_{c,i}$ and the mean size of bubbles D_b: $R_{o,i} = (1 - r_{c,i})\langle (A_{po}/\pi)^{0.5}/D_b \rangle D_b$, with $\langle (A_{po}/\pi)^{0.5}/D_b \rangle = \left[\frac{8}{14}(\frac{3\sqrt{3}}{2\pi})^{0.5} + \frac{6}{14}(\frac{1}{\pi})^{0.5}\right] 2^{1.5} \approx 0.27$. Moreover, closure ratio distributions shown in Fig. 4 allow us to calculate the fraction x_i of windows having an aperture size equal to R_i. Fig. 12 shows that the EM model predictions are in good agreement with experimental measurements and PUC computed values.

5. Conclusion

The work described in this paper investigates, both numerically and experimentally, the capability of millifluidic techniques to obtain light-weight cellular foams with tailored acoustical properties. The simple and yet versatile fabrication route proposed in this study consists in modifying the mass concentration of the polymeric solution, and it was shown that this approach allows bio-based solid cellular foams with controlled pore size and tuned membrane level to be obtained. The foam samples thus produced exhibit monodisperse pores with an assembly of closed and open windows, characterized by an appropriate aperture ratio. The dependence of the transport and sound absorbing properties on the membrane content was demonstrated. In particular, samples with increased sound absorption properties (visco-thermal losses) were successfully manufactured. The experimental evidence was further supported by computational results, in which the transport properties are predicted by combining multiscale simulations with an averaging procedure. The latter involves all independent configurations of the membrane content, identified using the experimental distribution. These results confirm the relevance of the fabrication strategy in the production of raw materials with optimal sound proofing capabilities. The combination of our improved understanding of the structure/property of rigid foams, together with the recently developed analysis of the acoustics of permeo-elastic materials [39], provides great scope for in-depth investigations of better absorption abilities of solid foams with thin membranes [40], and for the development of new foam materials with purpose designed properties.

Data availability

Data will be made available on request.

CRediT authorship contribution statement

Van Hai Trinh: Investigation, Writing - original draft, Writing - review & editing. **Vincent Langlois:** Formal analysis, Supervision, Writing - original draft, Writing - review & editing. **Johann Guilleminot:** Writing - original draft, Writing - review & editing, Supervision. **Camille Perrot:** Formal analysis, Supervision, Writing - original draft, Writing - review & editing, Funding acquisition. **Yacine Khidas:** Writing - review & editing, Resources. **Olivier Pitois:** Writing - review & editing, Resources, Funding acquisition, Project administration.

Acknowledgments

This work was part of a project supported by ANR (Grants No. ANR-13-RMNP-0003-01 and No. ANR-13-RMNP-0003-03). The work of V. H. Trinh was supported by a fellowship awarded by the Government of Vietnam (Project 911).

Appendix A. Reconstruction of periodic unit cell

In this appendix, we focus on the calculation of the geometrical parameters, porosity ϕ and thermal characteristic length Λ', associated with the idealized foam geometry considered in this work. As the porosity depends on the volume of pore-space and the thermal characteristic length depends on its surface, the effect of membranes on each parameter is very different. Due to the low thickness of membranes, their volume is negligible compared to the volume of ligaments and vertices. Therefore, the calculation of porosity can be performed on a cell containing no membrane. In the following, we consider this configuration as a starting point, and we then focus on

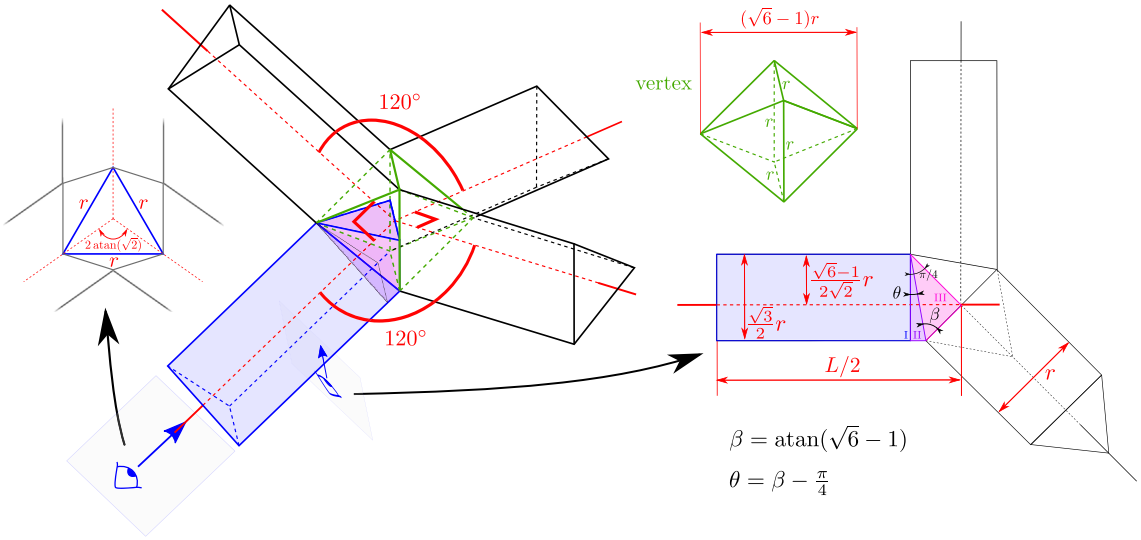

Fig. 15. Detail of an interconnection of four half-ligaments in the Kelvin cell.

the effect of membrane surface on the thermal characteristic length, Λ'.

At first, let us consider the case of a fully open cell (containing no membrane) having a Kelvin structure. The cell structure is then made of 24 ligaments and 12 vertices, all identical to each other. Fig. 15 shows an interconnection of four half-ligaments. Note that, in the Kelvin cell, the angles between ligaments are not equal to the tetrahedral angle (≈109.5°) and have not all the same value: two angles are right (to form a square window), and two angles are equal to 120° (to form a hexagonal window). Moreover, due to the chosen shape of ligaments, each half-ligament is a truncated triangular prism and the vertex is an irregular octahedron.

The total solid volume over the unit cell is equal to the volume of 48 half-ligaments,

$$V_{solid} = 24 \times 2 \times (V_{lig} + V_{ver}), \tag{A.1}$$

where $V_{lig} = V_I + V_{II}$ and $V_{ver} = V_{III}$ with,

$$V_I = \frac{\sqrt{3}}{4} r^2 \left(\frac{L}{2} - r\frac{\sqrt{6}-1}{2\sqrt{2}} \right), \quad V_{II} = \frac{r^3}{4}\tan\theta, \text{ and } V_{III} = \frac{\sqrt{6}-1}{12} r^3. \tag{A.2}$$

Then, the porosity of the open cell structure is calculated as follows

$$\phi = 1 - \frac{V_{solid}}{D_b^3} = 1 - \frac{3\sqrt{3}}{\sqrt{2}} \left(\frac{r}{D_b} \right)^2 + C_\phi \left(\frac{r}{D_b} \right)^3, \tag{A.3}$$

with $C_\phi = 10 - 3\sqrt{6}$.

Note that the previous calculation is valid until the opposite ligaments of a window interact with each other leading to the closure of square windows. Therefore, the following conditions on the ligament width or on the porosity ϕ require that: $\frac{r}{D_b} \geq \frac{1}{2(\sqrt{6}-1)}$ (closure of squares) or $\phi \geq 0.67$. By considering Eq. (A.3), it is possible to estimate the width of ligaments from the porosity as follows:

$$\frac{r}{D_b} = \sqrt{\frac{1-\phi}{\frac{3\sqrt{3}}{\sqrt{2}} - C_\phi \frac{r}{D_b}}} \approx \sqrt{\frac{1-\phi}{\frac{3\sqrt{3}}{\sqrt{2}} - C_\phi \sqrt{\frac{(1-\phi)\sqrt{2}}{3\sqrt{3}}}}}. \tag{A.4}$$

Now, we focus on the calculation of the thermal characteristic length defined as $\Lambda' = 2V_p/A_p$ where V_p and A_p are respectively the volume and the surface of the pore-space. The thermal characteristic length is directly linked to the specific surface $S_p = A_p/D_b^3$ leading to $\Lambda'/D_b = 2\phi/(S_p D_b)$. In the case of a fully open cell, the surface of the pore-space is the surface of the ligaments and vertices. By considering the surfaces of triangular prisms and those of tetrahedra, we obtain after some calculations:

$$S_{p,o} D_b = \frac{A_{p,o}}{D_b^2} = \frac{36r}{\sqrt{2}D_b} + C_{s,0}\frac{r^2}{D_b^2}, \tag{A.5}$$

with $C_{s,0} = 12\sqrt{2}\left[\sqrt{4-\sqrt{6}} - (\sqrt{6}+1)\right]$.

For a cell having some membranes, we must consider their surface, $A_{membrane}$, which depends on the closure ratio of hexagonal and square windows, $r_{c,he}$ and $r_{c,sq}$,

$$S_p D_b = \frac{A_{p,o}}{D_b^2} + \frac{A_{membrane}}{D_b^2}, \tag{A.6}$$

where $A_{membrane} = \sum_{i=1}^{6} A_{c,sq,i} + \sum_{j=1}^{8} A_{c,he,j}$ with

$$A_{c,sq,i} = 2L^2 \left[\left(1 - \frac{\sqrt{6}-1}{\sqrt{2}} \frac{r}{L} \right)^2 - (1 - r_{c,sq,i})^2 \right], \tag{A.7a}$$

$$A_{c,he,j} = 3\sqrt{2}L^2 \left[\left(1 - \frac{1}{\sqrt{2}} \frac{r}{L} \right)^2 - (1 - r_{c,he,j})^2 \right]. \tag{A.7b}$$

After some computations, we obtain:

$$S_p D_b = \left[\frac{3}{2} + 3\sqrt{3} + C_{s,1}\frac{r}{D_b} + C_{s,2}\left(\frac{r}{D_2} \right)^2 \right] - \left[\frac{N_v}{4} x_o^{sq} (1 - r_{c,sq})^2 + \frac{3\sqrt{3}N_v}{8} x_o^{he} (1 - r_{c,he})^2 \right], \tag{A.8}$$

with $C_{s,1} = 6\left(1 + 3\sqrt{2} - 2\sqrt{3} - \sqrt{6}\right)$ and $C_{s,2} = 6\left(7 + \sqrt{32 - 8\sqrt{6}} - \sqrt{8} - \sqrt{12} - \sqrt{24}\right)$.

The terms within the first brackets are related to the specific surface of a fully closed cell, and the ones in the second brackets are related to the aperture surface of windows.

Then, from the previous calculation, we deduce the expression of the thermal characteristic length, Λ':

$$\frac{D_b}{\Lambda'} = \frac{D_b}{\Lambda'_c}\frac{\phi_c}{\phi} - \frac{N_v}{8\phi}x_o^{sq}(1-r_{c,sq})^2 - \frac{3\sqrt{3}N_v}{16\phi}x_o^{he}(1-r_{c,he})^2, \tag{A.9}$$

where Λ'_c and $\phi_c(\approx \phi)$ are respectively the thermal characteristic length and the porosity of a fully closed cell.

For the case of a PUC with an identical closure ratio of membrane r_c, we obtain,

$$\frac{D_b}{\Lambda'} = \frac{D_b}{\Lambda'_c}\frac{\phi_c}{\phi} - \frac{N_v}{\phi}\left(\frac{1}{8}x_o^{sq} + \frac{3\sqrt{3}}{16}x_o^{he}\right)(1-r_c)^2, \tag{A.10}$$

with

$$\frac{D_b}{\Lambda'_c} = \frac{1}{2\phi_c}\left[\frac{3}{2} + 3\sqrt{3} + C_{s,1}\frac{r}{D_b} + C_{s,2}\left(\frac{r}{D_2}\right)^2\right]. \tag{A.11}$$

By calculating the thermal characteristic length Λ'_c of a fully closed cell for various values of the porosity using the previous equation, we found that the ratio Λ'_c/D_b is almost constant in the range of porosity [0.67; 1]: $\Lambda'_c/D_b \approx 0.3 \pm 0.02$.

Appendix B. Global calculation of equivalent configurations

We consider the response of a system defined in Section 3.1. Specifically, we wish to show that, for the particular case at hand in which the reconstruction of real foams is addressed by means of both the number of closed windows and the size of window aperture, a drastic reduction of the number of calculations to be considered can be obtained. This calculation is carried out in an iterative way and consists of browsing the graph of linked configurations with the aim to define a set of equivalent configurations, Fig. 11b. At the beginning of the iterative process, the first line of the table found at the end of the step III is used as a starting equivalent configurations list. All configurations associated with the configurations from the starting list are added to it to build a new list of equivalent configurations. This list becomes the starting list in the iterative process. As previously, this list is used to build a new list, etc. The process is repeated until the starting list and the recalculated list are equal. At the end of the iterative process, the set of configurations equivalent to the first one is identified. Then, the calculation is repeated with a line which has still not been visited. When all configurations have been visited, the calculation is finished. The major steps in the equivalent configurations calculation are summarized in Fig. 11.

References

[1] W. Zhai, X. Yu, X. Song, L.Y.L. Ang, F. Cui, H.P. Lee, T. Li, Microstructure-based experimental and numerical investigations on the sound absorption property of open-cell metallic foams manufactured by a template replication technique, Mater. Des. 137 (2018) 108–116.

[2] J.G. Gwon, S.K. Kim, J.H. Kim, Sound absorption behavior of flexible polyurethane foams with distinct cellular structures, Mater. Des. 89 (2016) 448–454.

[3] E.T. Bird, A.E. Bowden, M.K. Seeley, D.T. Fullwood, Materials selection of flexible open-cell foams in energy absorption applications, Mater. Des. 137 (2018) 414–421.

[4] N.C. Hilyard, A. Cunningham, Low Density Cellular Plastics: Physical Basis of Behaviour, Chapman & Hall, London, 1994.

[5] L.J. Gibson, M.F. Ashby, Cellular Solids: Structure and Properties, Cambridge University Press, Cambridge, 1997.

[6] A. Testouri, M. Ranft, C. Honorez, N. Kaabeche, J. Ferbitz, D. Freidank, W. Drenckhan, Generation of crystalline polyurethane foams using millifluidic lab-on-a-chip technologies, Adv. Eng. Mater. 15 (2013) 1086–1098.

[7] J. Allard, N. Atalla, Propagation of Sound in Porous Media: Modeling Sound Absorbing Materials, 2nd ed. ed., John Wiley & Sons, Chichester, 2009.

[8] D.L. Johnson, J. Koplik, R. Dashen, Theory of dynamic permeability and tortuosity in fluid-saturated porous media, J. Fluid Mech. 176 (1987) 379–402.

[9] D. Lafarge, P. Lemarinier, J.F. Allard, V. Tarnow, Dynamic compressibility of air in porous structures at audible frequencies, J. Acoust. Soc. Am. 102 (1997) 1995–2006.

[10] D. Westhoff, J. Skibinski, O. Šedivý, B. Wysocki, T. Wejrzanowski, V. Schmidt, Investigation of the relationship between morphology and permeability for open-cell foams using virtual materials testing, Mater. Des. 147 (2018) 1–10.

[11] Y. Champoux, J.F. Allard, Dynamic tortuosity and bulk modulus in air-saturated porous media, J. Appl Phys. 70 (1991) 1975–1979.

[12] R. Panneton, X. Olny, Acoustical determination of the parameters governing viscous dissipation in porous media, J. Acoust. Soc. Am. 119 (2006) 2027–2040.

[13] X. Olny, R. Panneton, Acoustical determination of the parameters governing thermal dissipation in porous media, J. Acoust. Soc. Am. 123 (2008) 814–824.

[14] M.A. Biot, Theory of propagation of elastic waves in a fluid-saturated porous solid, I. Low-frequency range, J. Acoust. Soc. Am. 28 (1956) 168–178.

[15] J.F. Allard, Y. Champoux, New empirical equations for sound propagation in rigid frame fibrous materials, J. Acoust. Soc. Am. 91 (1992) 3346–3353.

[16] C. Boutin, C. Geindreau, Periodic homogenization and consistent estimates of transport parameters through sphere and polyhedron packings in the whole porosity range, Phys. Rev. E 82 (2010) 036313.

[17] I. Malinouskaya, V. Mourzenko, J.F. Thovert, P. Adler, Wave propagation through saturated porous media, Phys. Rev. E 77 (2008) 066302.

[18] C. Peyrega, D. Jeulin, Estimation of acoustic properties and of the representative volume element of random fibrous media, Z. Appl. Phys 113 (2013) 104901.

[19] S. Gasser, F. Paun, Y. Bréchet, Absorptive properties of rigid porous media: application to face centered cubic sphere packing, J. Acoust. Soc. Am. 117 (2005) 2090–2099.

[20] O. Doutres, N. Atalla, K. Dong, A semi-phenomenological model to predict the acoustic behavior of fully and partially reticulated polyurethane foams, J. Appl. Phys 113 (2013) 054901.

[21] J.H. Park, K.S. Minn, H.R. Lee, S.H. Yang, C.B. Yu, S.Y. Pak, C.S. Oh, Y.S. Song, Y.J. Kang, J.R. Youn, Cell openness manipulation of low density polyurethane foam for efficient sound absorption, J. Sound Vib. 406 (2017) 224–236.

[22] K. Gao, J.A.W. van Dommelen, M.G.D. Geers, Microstructure characterization and homogenization of acoustic polyurethane foams: measurements and simulations, Int. J. Solids Struct. 100 (2016) 536–546.

[23] M.T. Hoang, G. Bonnet, H.T. Luu, C. Perrot, Linear elastic properties derivation from microstructures representative of transport parameters, J. Acoust. Soc. Am. 135 (2014) 3172–3185.

[24] M.T. Hoang, C. Perrot, Solid films and transports in cellular foams, J. Appl. Phys. 112 (2012) 054911.

[25] E. Lorenceau, N. Louvet, F. Rouyer, O. Pitois, Permeability of aqueous foams, Eur. Phys. J. E 28 (2009) 293–304.

[26] Y. Khidas, B. Haffner, O. Pitois, Critical size effect of particles reinforcing foamed composite materials, Compos. Sci. Technol. 119 (2015) 62–67.

[27] I. Cantat, S. Cohen-Addad, F. Elias, F. Graner, R. Höhler, O. Pitois, F. Rouyer, A. Saint-Jalmes, Foams: Structure and Dynamics, Oxford University Press Oxford. 2013.

[28] L. Gong, S. Kyriakides, W.Y. Jang, Compressive response of open-cell foams. Part I: morphology and elastic properties, Int. J. Solid. Struct. 42 (2005) 1355–1379.

[29] A.M. Kraynik, D.A. Reinelt, F. van Swol, Structure of random monodisperse foam, Phys. Rev. E 67 (2003) 031403.

[30] Y. Salissou, R. Panneton, Wideband characterization of the complex wave number and characteristic impedance of sound absorbers, J. Acoust. Soc. Am. 128 (2010) 2868–2876.

[31] S. Torquato, Relationship between permeability and diffusion-controlled trapping constant of porous media, Phys. Rev Lett. 64 (1990) 2644.

[32] C. Perrot, R. Panneton, X. Olny, Periodic unit cell reconstruction of porous media: application to open-cell aluminum foams, J. Appl. Phys. 101 (2007) 113538.

[33] C. Perrot, F. Chevillotte, M.T. Hoang, G. Bonnet, F.-X. Bécot, L. Gautron, A. Duval, Microstructure, transport, and acoustic properties of open-cell foam samples: experiments and three-dimensional numerical simulations, J. Appl. Phys. 111 (2012) 014911.

[34] J. Park, S.H. Yang, K.S. Minn, C.B. Yu, S.Y. Pak, Y.S. Song, J.R. Youn, Design and numerical analysis of syntactic hybrid foam for superior sound absorption, Mater. Des. 142 (2018) 212–220.

[35] V. Langlois, V.H. Trinh, C. Lusso, C. Perrot, X. Chateau, Y. Khidas, O. Pitois, Permeability of solid foam: effect of pore connections, Phys. Rev. E 97 (2018) 053111.

[36] J.L. Auriault, C. Boutin, C. Geindreau, Homogenization of Coupled Phenomena in Heterogenous Media, John Wiley & Sons, New York, 2009.

[37] M. Avellaneda, S. Torquato, Rigorous link between fluid permeability, electrical conductivity, and relaxation times for transport in porous media, Phys. Fluids A-Fluid 3 (1991) 2529–2540.

[38] J. Rubinstein, S. Torquato, Diffusion-controlled reactions: mathematical formulation, variational principles, and rigorous bounds, J. Chem. Phys. 88 (1988) 6372–6380.

[39] R. Venegas, C. Boutin, Acoustics of permeo-elastic materials, J. Fluid Mech. 828 (2017) 135–174.

[40] C. Gaulon, J. Pierre, C. Derec, L. Jaouen, F.-X. Bécot, F. Chevillotte, F. Elias, W. Drenckhan, V. Leroy, Acoustic absorption of solid foams with thin membranes, Appl. Phys. Lett. 112 (2018) 261904.